

https://dspace.org/

Elastic scattering and inelastic excitation of an unbound state in the fermionic 9Be + 9Be system near the Coulomb barrier

Mayida, Innocent

2011-07-20
http://hdl.handle.net/10539/10302

Downloaded from a DSpace repository. https://dspace.org/

ELASTIC SCATTERING AND INELASTIC EXCITATION OF AN UNBOUND STATE IN THE FERMIONIC ^{9}Be + ^{9}Be SYSTEM NEAR THE COULOMB BARRIER

by

Innocent Mayida

A Research Report submitted to the Faculty of Science, University of the Witwatersrand, Johannesburg, in partial fulfilment of the requirements for the degree of Master of Science.

Johannesburg 2011

Declaration

I declare that this Research Report is my own, unaided work. It is being submitted for the partial fulfilment of the requirements for the degree of Master of Science in the University of the Witwatersrand, Johannesburg. It has not been submitted before for any degree or examination in any other University.

Signature:. 

Student name: Innocent Mayida

Date: May 2011.

Abstract

The angular distributions for elastic and, at the highest incident energy, inelastic scattering to the particle-unbound excited state $^{9}Be^{*}(5/2^{-}, 2.430$ MeV) in ^{9}Be have been measured in the scattering system $^{9}Be + ^{9}Be$ at $E_{Lab} = 9$, 12 and 16 MeV. In addition, elastic and inelastic scattering excitation-functions for the $^{9}Be + ^{9}Be$ system were measured at two different scattering angles ($\theta_{c.m.} = 90°$ and 50°), over an incident energy range $6 \leq E_{Lab} \leq 25$ MeV. The inelastic scattering cross-sections can be measured by detecting the corresponding recoil nucleus in the scattering process. The experimental work was performed using the 6 MV EN tandem Van de Graaff accelerator at iThemba LABS (Gauteng). The scattered elastic and inelastic ^{9}Be were detected by the ΔE-E gas-ionisation detector and the CAMAC + WIMPS2 data acquisition was used to identify the scattered particles online. Optical model calculations were carried out in order to fit the elastic scattering data and determine an energy-independent optical model potential. Distorted Wave Born Approximation (DWBA) was used to analyse the inelastic scattering with the extracted deformation length, δ_2, being in agreement with previous measurements.

Dedication

To Tarie for the “time endured”

Acknowledgements

I am heartily thankful to my supervisor, Prof. J. Carter, whose encouragement, guidance and support from the initial to the final level enabled me to develop an understanding of the subject.

It is difficult to overstate my gratitude to my co-supervisor Prof. E. Sideras-Haddad. With his enthusiasm, his inspiration, and his great effort to explain things clearly and simplify, he helped to make nuclear physics fun for me. He provided sound advice, good teaching, good company, and lots of ideas. I would have lost without him.

I am also grateful to iThemba LABS (Gauteng) and the university of Witwatersrand for the financial support during my work.

I am indebted to my student colleagues, and friends for providing, a stimulating and fun environment in which to learn and grow. However, because the list might be too long and by fear of leaving someone out, I will simply say, "*Thank you very much to you all"*.

My deepest gratitude, to the iThemba LABS (Gauteng) accelerator staff, Dr M. Madhuku, Mr O. Pekah, Mr F. Balzan and Mr G. Badenhorst for the running of the Nuclear Physics experiments.

Thanks to the iThemba LABS (Gauteng) staff for assisting me in many ways. Ms D Mahlare, Ms D. Monyamane and Ms N. Radebe deserve a special mention.

To my life-long friend Tariro, who has been, always, my pillar, my joy and my guiding light. *Thank you!*

Table of Contents

Declaration.....(i)
Abstract.....(ii)
Dedication.....(iii)
Acknowledgements.....(iv)
Table of contents.....(v)
List of Figures.....(vii)
List of Tables.....(x)
Chapter 1 - Introduction.....1

Chapter 2 - Theoretical Considerations.....4
2.1 Coulomb scattering.....4
2.1.1 Rutherford scattering.....4
2.1.2 Mott scattering.....6
2.2 Optical Model of Elastic scattering.....7
2.1.2 Extension of the Optical Model for identical particles.....7
2.3 DWBA for inelastic scattering.....12

Chapter 3 - Experimental Details, Data Extraction.....15
3.1 Beam production and transportation.....15
3.1.1 Inflection magnet.....16
3.1.2 Targets.....16
3.2 Experimental set up.....16
3.3 Δ*E*-*E* detector.....19
3.4 Data Acquisition system and data extraction.....21
3.5 Energy resolution of the detector system.....26
3.6 Determinations of scattering cross-sections.....28
3.9 Review of elastic scattering data.....32
Chapter 4 – Analysis and discussion..........36
4.1 Introduction.....36
4.2 Effect on intrinsic spin identical particle system.....36
4.3 Optical model analysis of elastic scattering.....37

4.3.1 Parameter set C-1.and W-1.....38
4.3.2 Parameter set W-2.....39
4.3.3 Parameter set W-3.....39
4.3.4 Parameter set W-4 and elastic scattering excitation functions.....39
4.4 DWBA analysis for inelastic scattering to $^{9}Be^{*}(5/2^{-}$, 2.43 MeV).....46
4.5 Discussion.....50
Chapter 5 - Summary and Conclusion.....52
References.....54
Appendix A- Tabulated values of the measured Quantities.....57
Appendix B York *et al*. 71

List of Figures

Figure 2.1: Coulomb trajectory for Rutherford scattering.....5

Figure 2.2: Indistinguishable which may occur when two identical particles collide.....7

Figure 3.1: The extracted negative ions after an inflection magnet scan.....17

Figure 3.2: The schematic diagram for the C-line and associated equipment at the EN Tandem accelerator of iThemba LABS (Gauteng.....18

Figure 3.3: A schematic diagram of the ΔE-E gas-ionisation gas delivery system.....20

Figure 3.4: Block diagram of the data acquisition system.....22

Figure 3.5: Two dimensional ΔE-E spectrums of ^{9}Be + ^{9}Be at E_{Lab} = 16 MeV and θ_{Lab} = 25 24

Figure 3.6: One dimensional ΔE-E spectrums of ^{9}Be + ^{9}Be at E_{Lab} = 16 MeV and θ_{Lab} = 25°.....25

Figure 3.7: Angular distributions of elastic scattering for ^{9}Be + ^{9}Be at E_{Lab} = 5, 9, 12 and 16 MeV including data from York and Carpenter [YO77].....30

Figure 3.8: Angular distributions for the elastic scattering of ^{9}Be + ^{9}Be at E_{Lab} = 16 MeV and inelastic excitation of second unbound state ^{9}Be($5/2^{-}$, 2.43 MeV).....31

Figure 3.9: Excitation functions for the elastic scattering of ^{9}Be + ^{9}Be at $\theta_{c.m.}$ = 90° and 50°.....32

Figure 3.10: Excitation functions for the elastic and inelastic excitations scattering of ^{9}Be + ^{9}Be at $\theta_{c.m.}$ = 90° and $\theta_{c.m.} \approx$ 90°.....33

Figure 3.11: Excitation functions for the elastic and inelastic scattering of ^{9}Be + ^{9}Be at $\theta_{c.m.}$ = 50° and $\theta_{c.m.} \approx$ 50°.....34.

Figure 4.1: Angular distributions of elastic scattering for ^{9}Be + ^{9}Be showing the influence of different intrinsic spin values on Mott scattering cross-sections.....37

Figure 4.2: Angular distributions for the elastic scattering of ^{9}Be + ^{9}Be at E_{Lab} = 5, 9, 12 and 16 MeV using C-1 and W-1.....41

Figure 4.3: Angular distributions for the elastic scattering of ^{9}Be + ^{9}Be at E_{Lab} = 5, 9, 12 and 16 MeV using W-2 potential.....42

Figure 4.4: Angular distributions for the elastic scattering of ^{9}Be + ^{9}Be at E_{Lab} = 5, 9, 12 and 16 MeV using W-3 potential.....43

Figure 4.5: Angular distributions for the elastic scattering of ^{9}Be + ^{9}Be at E_{Lab} = 5, 9, 12 and 16 MeV using W-4 potential.....44

Figure 4.6: Excitation functions for the elastic scattering of ^{9}Be + ^{9}Be at $\theta_{c.m.}$ = 90° and 50°.....45

Figure 4.7: Angular distributions for the elastic scattering of ^{9}Be + ^{9}Be at E_{Lab} = 16 MeV and inelastic excitation of second unbound state ^{9}Be*(5/2^{-} , 2.43 MeV).....47

Figure 4.9: Elastic and inelastic excitation for the ^{9}Be + ^{9}Be system at $\theta_{c.m.} = 90°$ and $\theta_{c.m.} \approx 90°$ (DWBA).....48

Figure 4.9: Elastic and inelastic excitation for the ^{9}Be + ^{9}Be system at $\theta_{c.m.} = 50°$ and $\theta_{c.m.} \approx 50°$ (DWBA).....49

List of Tables

Table 3.1: Best operating conditioning conditions for the ΔE gas-ionisation detector determined using iso-butane gas at a differential pressure of 1k Pa.....21

Table 3.2: Measured data for ^{9}Be + ^{9}Be scattering at incident energies just above the Coulomb barrier.....29

Table 4.1: Optical Model parameters searching for ^{9}Be +^{9}Be 40

Table A1: Elastic scattering of ^{9}Be + ^{9}Be at E_{Lab} = 16 MeV.....58

Table A2: Elastic scattering of ^{9}Be + ^{9}Be at E_{Lab} = 16 MeV (scaled).....59

Table A3: Excitations functions of ^{9}Be + ^{9}Be at $\theta_{\mathrm{c.m.}}$ = 50° 60

Table A4: Excitations functions of ^{9}Be + ^{9}Be at $\theta_{\mathrm{c.m.}}$ = 90° 61

Table A5: Inelastic scattering ^{9}Be at E_{Lab} = 16 MeV 62

Table A6: Inelastic scattering ^{9}Be at E_{Lab} = 16 MeV (scaled).....63

Table A7: Elastic scattering of ^{9}Be + ^{9}Be at E_{Lab} = 12 MeV.....64

Table A8: Elastic scattering of ^{9}Be + ^{9}Be at E_{Lab} = 12 MeV (scaled).....65

Table A9: Elastic scattering of ^{9}Be + ^{9}Be at E_{Lab} = 12 MeV.....66

Table A10: Elastic scattering of ^{9}Be + ^{9}Be at E_{Lab} = 12 MeV (scaled).....67

Table A11: Elastic scattering of ^{9}Be + ^{9}Be at E_{Lab} = 9 MeV.....68

Table A12: Elastic scattering of ^{9}Be + ^{9}Be at E_{Lab} = 9 MeV (scaled).....69

Table A13: Elastic scattering of ^{9}Be + ^{9}Be at E_{Lab} = 5 MeV (YO77) 70

Chapter 1

Introduction

The main part of this research report is concerned with an experimental investigation of elastic and inelastic scattering to the particle-unbound state ($5/2^-$, 2.430 MeV) of ^{9}Be at energies near the Coulomb barrier. In a scattering experiment of a light heavy-ion reaction, vital information i.e. the size of the nucleus and the characteristics of the nuclear force can be obtained [SA80].The ^{9}Be + ^{9}Be scattering, as a light heavy-ion reaction, has previously been studied experimentally [YO77], [UN79]. The ^{9}Be + ^{9}Be system is fermionic (half integer spin, $3/2^-$ ground state). Scattering systems which involve the ^{9}Be nucleus display a strong presence of coupling effects [MU94]. The elastic and inelastic scattering cross-sections are strongly influenced by the ease with which ^{9}Be breaks into 2α + *n* at E_x = 1.57 MeV. The ^{9}Be nucleus has a low-lying state that can be excited easily by inelastic scattering. The immediate break-up on excitation of the ^{9}Be nucleus prevents direct detection, and only the corresponding recoil nucleus can be used for determining the inelastic-scattering cross-sections. The present study was carried out in order to further investigate the interaction of loosely bound nuclei**,** and inelastic excitation of an unbound state of ^{9}Be.

The Coulomb scattering is developed as the Mott cross-section being an extension of the more familiar Rutherford cross-section for identical particle scattering. In heavy-ion scattering systems in which the projectile and the target are identical, they are indistinguishable after the elastic scattering has taken place, and so the differential cross-section is symmetric about $\theta_{c.m.} = 90°$. The role of the spin, *I*, was investigated in the entrance channel of elastic scattering, for the Mott cross-section of the ^{9}Be + ^{9}Be system. The inelastic scattering to the second, unbound, state excited in a 2-body interaction which breaks up later (E_x = 2.430 MeV, $J^\pi = 5/2^-$) has received very little attention and mostly at incident energies far above the Coulomb barrier [MU94], [MU95] and [OM84]. The present study concentrates on measurements and interpretations of the inelastic scattering cross-sections for

unbound ^{9}Be at $\theta_{\text{c.m.}} \approx 90°$ and 50° near the Coulomb barrier. The inelastic excitation proceeds from a $J^{\pi} = 0^{+}$ ground state to a $J^{\pi} = 2^{+}$ excited state involving an angular momentum $\Delta L = 2\ \hbar$. Therefore, the excitation from ^{9}Be ($3/2^{-}$, g.s.) to the rotational second, unbound, state ^{9}Be*($5/2^{-}$, 2.430 MeV) can be replaced by the excitation of the core from ground state ^{9}Be (0^{+}, g.s.) to the excited state ^{9}Be *(2^{+}, 2.430 MeV).

The optical model [FE54] has been used successfully in the description of elastic scattering data. The optical model was used for all the elastic scattering data analysis. Inelastic scattering analysis was carried using the Distorted-Wave Born Approximation (DWBA), using an elastic scattering optical potential to generate the distorted waves of relative motion. Previously, an energy-dependent optical potential was obtained from very limited elastic scattering data measured by York *et al*. [YO77]. The aim of this present investigation is to significantly extend the ^{9}Be + ^{9}Be scattering data at and just above the Coulomb barrier ($E_{\text{Lab}}^{\text{CB}} = 8.0$ MeV). As such, it is expected that an energy-independent optical potential can be extracted which is valid over the relatively small incident energy region of $5 \leq E_{\text{lab}} \leq 25$ MeV.

Experimentally the ^{9}Be ion beams produced by the sputter source were accelerated to the desired energies with a 6 MV EN tandem Van de Graaff at iThemba LABS (Gauteng). The elastically and inelastically scattered ^{9}Be were detected by a high resolution ΔE-E gas-ionisation detector and the CAMAC + WIMPS2 data acquisition was used to identify the particles online.

The layout of this research report is as follows:

- Chapter 2 describes the theoretical considerations and the models used for data analysis.

- Chapter 3 presents the experimental details of the study and data extraction. An outline on how the experimental apparatus was used is

detailed here and a review of the elastic and inelastic scattering data (present and previous).

- Chapter 4 presents the analysis of the results of elastic and inelastic scattering of ^{9}Be + ^{9}Be. The Mott and Rutherford scattering formulae in relation to the Optical Model and DWBA are also detailed in this chapter.

- Chapter 5 presents the summary and conclusion.

- Appendices, with tabulated measured results are found at the back of the research report.

Chapter 2

Theoretical considerations

The nucleus–nucleus interaction remains a complex scenario in nuclear structure studies and this can be solved by a systematic analysis of experimental data using different theoretical methods. The Optical Model (OM) provides a lot of information on nucleus–nucleus interactions and is based on the structure of the nuclei and the Coulomb interaction energy. Coulomb scattering is as a result of the electric field between charged particles. For non-identical particles Rutherford scattering occurs and for the identical particles Mott scattering results [BE64].

2.1 Coulomb scattering

Scattering experiments are used as a basic tool for understanding the nucleus in its ground state and excited states. Considering two-body reactions, many different processes may take place when two particles collide [SA80]. Reactions between an incident nucleus, *a*, and target nucleus, *A*, produces a target-related recoil nucleus, *B*, and a projected nucleus, *b* and may be described as follows:

$$a + A \rightarrow b + B \quad \text{or} \quad A(a,b)B\,. \tag{2.1}$$

In addition, an amount of energy, *Q*, may be released during the reaction or may be required by the reaction. This is referred to as the *Q*-value and for elastic scattering $Q = 0$, the projectile and target nuclei retain their identity and Eq. (2.1) becomes $A(a,a)A$.

2.1.1 Rutherford scattering

When a charged particle collides with a nucleus the scattered particles follows a hyperbolic path and in this case for the unbound orbit is constrained by a $1/r^2$ forces [KR88] as shown in Fig. 2.1. Charged particle scattering is referred to as elastic Coulomb scattering (Rutherford scattering) [JE90]. Asymptotically, the

projectile approaches a target nucleus along a straight line at a distance b from a line to the scattering centre (see Fig. 2.1). Classically, the projectile is scattered by the Coulomb field of the target by an angle θ_{Lab}. The Coulomb force is long ranged and hence it cannot be neglected, even at large separations. As it approaches the target, it reaches a separation distance r_{min} which depends on the impact parameter b. When $b = 0$ a head-on collision occurs and the projectile reverses its motion and at the distance of closest approach, d, the initial projectile kinetic energy is converted to Coulomb potential energy.

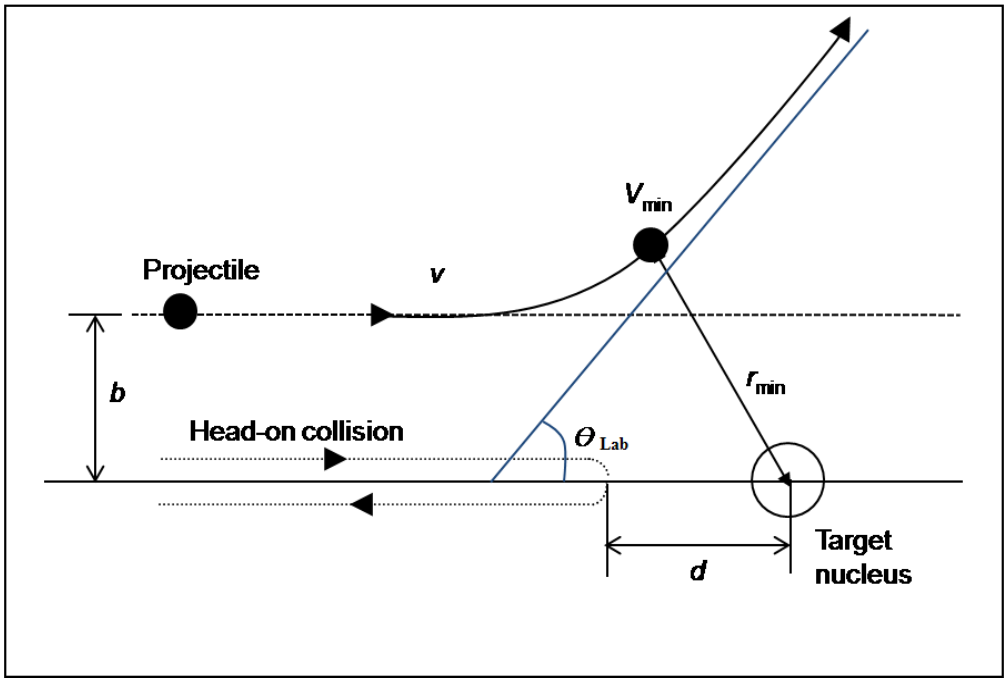


Figure 2.1: Coulomb trajectory for Rutherford scattering.

Non-identical particle scattering yields the Rutherford scattering formula for Coulomb scattering [KR88].

$$\frac{d\sigma}{d\Omega_{\text{c.m.}}} = \left(\frac{Z_1 Z_2 e^2}{4\pi\varepsilon_0}\right)^2 \left(\frac{1}{4E_{\text{c.m.}}}\right)^2 \left(\frac{1}{\sin^4\theta_{\text{c.m.}}/2}\right), \tag{2.2}$$

where $Z_1 e$ is the projectile charge, $Z_2 e$ is the target charge, $E_{\text{c.m.}}$ is the projectile centre-of-mass energy and $\theta_{\text{c.m.}}$ is the centre-of-mass scattering angle.

2.1.2 Mott scattering

Considering scattering of identical particles, the wave function describing the relative motion must be symmetric for even-*A* (bosonic systems) and asymmetric for odd-*A* (fermionic systems) under the interchange of any two indistinguishable particles contained in it [SA80]. When the intrinsic spin *I* of the particle is greater than zero, the exchange symmetry of the spin part of the wave function must be considered. If the interacting ions are identical, they are indistinguishable after the elastic scattering has taken place, and so the differential cross-section is symmetric about $\theta_{\text{c.m.}} = 90°$ [HO78]. Quantum theory introduces interference and the interaction is as illustrated in Fig. 2.2. Classically, the observed cross-section would be the sum of the cross-section of the two possibilities [HO78]:

$$\frac{d\sigma}{d\Omega_{\text{c.m.}}} = \frac{d\sigma(\theta_{\text{c.m.}})}{d\Omega_{\text{c.m.}}} + \frac{d\sigma(\pi - \theta_{\text{c.m.}})}{d\Omega_{\text{c.m.}}}. \tag{2.3}$$

However, it becomes necessary to add the amplitudes, and the symetrised elastic scattering cross-section is given by [AU78]:

$$\frac{d\sigma}{d\Omega_{\text{c.m.}}} = \left| f(\theta_{\text{c.m.}}) + f(\pi - \theta_{\text{c.m.}}) \right|^2 \tag{2.4a}$$

$$= \frac{d\sigma(\theta_{\text{c.m.}})}{d\Omega_{\text{c.m}}} + \frac{d\sigma(\pi - \theta_{\text{c.m.}})}{d\Omega_{\text{c.m.}}} + 2Real(f(\theta_{\text{c.m.}}) f(\pi - \theta_{\text{c.m.}})^*). \tag{2.4b}$$

The symmetrised cross-section has a highly oscillatory structure due to the interference of the two scattering amplitudes and is again symmetric at $\theta_{\text{c.m.}} = 90°$ [SA80]. The interference term introduces the oscillations giving an analytical expression called Mott scattering results [MO30]. Using the Coulomb scattering of point charges, the Rutherford scattering formula may be extended to yield the Mott scattering formula for identical particles [HO78]:

$$\left.\frac{d\sigma}{d\Omega_{\text{c.m.}}}\right)_I = \frac{\eta^2}{4k^2}\left\{\csc^4\frac{\theta_{\text{c.m.}}}{2} + \sec^4\frac{\theta_{\text{c.m.}}}{2}\right.$$

$$+\frac{(-)^{2I}}{2I+1}2\cos\left(\eta\ln\tan^2\frac{\theta_{\text{c.m.}}}{2}\right)\csc^2\frac{\theta_{\text{c.m.}}}{2}\sec^2\frac{\theta_{\text{c.m.}}}{2}\Bigg\}, \tag{2.5}$$

where $\eta = Z_1 Z_2 \mu / \hbar^2 k$ is the Sommerfield parameter (dimensionless), k is the wave number and μ is the reduced mass. The third part of Eq. (2.5) is the interference term and depends on the spin *I* of the target and projectile.

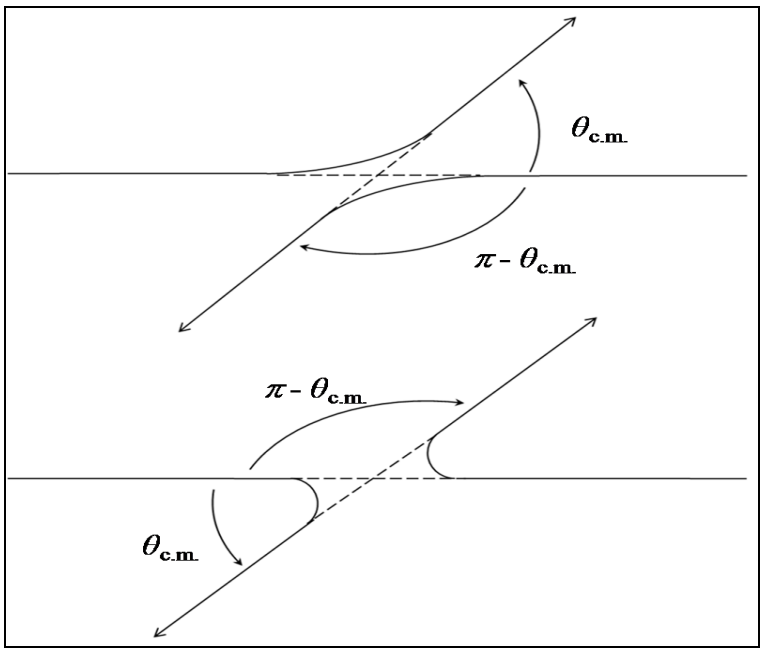


Figure 2.2: Indistinguishable events which may occur when two identical particles collide.

2.2 Optical Model of elastic scattering

The Optical Model (OM) of elastic scattering predicts elastic scattering in the presence of absorption effects, which may be of volume or surface nature. This model is analogous to the scattering of light by an absorbing sphere and is also called the "*cloudy crystal ball model*" [SA80]. The model incorporates an assumption that an imaginary part of the scattering potential accounts for the presence of inelastic scattering and reaction channels thus absorbing incident flux.

The Schrödinger equation for the scattering of charged nuclear particles incorporates a two-body interaction potential, $U(r)$, to represent the many-body interaction between the colliding nuclei [HO78]:

$$U(r) = U_{\mathrm{C}}(r) + U_{\mathrm{N}}(r), \tag{2.6}$$

where $U_{\mathrm{C}}(r)$ is the repulsive Coulomb interaction (long range) and $U_{\mathrm{N}}(r)$ is the attractive nuclear interaction (short range). The scattering potential $U_{\mathrm{N}}(r)$ is complex, with the general form:

$$U_{\mathrm{N}}(r) = [V(r) + iW(r)], \tag{2.7}$$

where V(r) is the real part responsible for elastic scattering and $iW(r)$ is the imaginary part responsible for absorption of flux from the elastic scattering channel.

A Woods-Saxon form [FE54] is generally chosen for the scattering potential of the heavy-ion scattering:

$$U_{\mathrm{N}}(r) = [V_0 f_{\mathrm{R}}(r) + iW_0 f_{\mathrm{I}}(r)], \tag{2.8a}$$

$$f_{\mathrm{R,I}}(r) = \left[1 + \exp\left(\frac{r - R_{\mathrm{R,I}}}{a_{\mathrm{R,I}}}\right)\right]^{-1}, \tag{2.8b}$$

where V_0 and W_0 represent the depths of the real and imaginary potentials, respectively. Here, $a_{\mathrm{R,I}}$ and $R_{\mathrm{R,I}}$ are the surface diffuseness and nuclear potential radii for the real and imaginary parts, respectively. The nuclear radii $R_{\mathrm{R,I}}$ are expressed in the following form for heavy ions:

$$R_{\mathrm{R,I}} = r_{0\mathrm{R,I}}(A_1^{1/3} + A_2^{1/3}), \tag{2.9}$$

whereas

$$R_{\mathrm{R,I}} = r_{0\mathrm{R,I}} A^{1/3} \tag{2.10}$$

for the light-ion convention with A_1 the mass of the projectile and A_2 being that of the target. The imaginary part of the nuclear potential described by Eq. (2.8a) and (2.8b) represents volume absorption and taking the first derivative,

$$W(r) = -\,W_{\mathrm{I}} \frac{d}{dr}\left[1+\exp\left(\frac{r-R_{\mathrm{I}}}{a_{\mathrm{I}}}\right)\right]^{-1}, \tag{2.11a}$$

$$= -\,W_1 4\exp\left(\frac{r-R_{\mathrm{I}}}{a_{\mathrm{I}}}\right)\Bigg/\left[1+\exp\left(\frac{r-R_{\mathrm{I}}}{a_{\mathrm{I}}}\right)\right]^{2}. \tag{2.11b}$$

When considering lower incident energies the Pauli Principle restricts the excitation of interior nucleons, resulting in an imaginary potential that is surface peaked [AU78]. The nuclear part of the optical potential can be obtained from measured elastic data [HA89].

The Coulomb potential, $U_{\mathrm{C}}(r)$, between the two interacting nuclei can be approximated for charged particle scattering as follows:

$$U_{\mathrm{C}}(r) = \frac{Z_1 Z_2 e^2}{r} \qquad , \mathrm{r} > R_{\mathrm{C}} \tag{2.12}$$

$$= \frac{Z_1 Z_2 e^2}{2R_{\mathrm{C}}}\left[3-\left(\frac{r^2}{R_{\mathrm{C}}^2}\right)\right] \qquad , \mathrm{r} \le R_{\mathrm{C}} \tag{2.13}$$

$$R_{\mathrm{C}} = \left[\frac{5}{3}\left\langle r^2 \right\rangle\right]^{\frac{1}{2}}, \tag{2.14}$$

where $\langle r^2 \rangle$ is the mean-square charge radius determined from electron scattering. The charge radius R_{C} is parametrised as:

$$R_{\mathrm{C}} = r_{0\mathrm{C}}(A_2^{1/3}), \tag{2.15}$$

where $r_{0\mathrm{C}}$ is the corresponding Coulomb-radius parameter.

By applying a partial wave expansion, in angular momentum to the solution of the Schrödinger equation, the radial wave-equation becomes [JA70]:

$$\left\{\frac{d^2}{dr^2}+k^2\left(1-\frac{U(r)}{E}\right)-\frac{\ell(\ell+1)}{r^2}\right\} f_\ell(kr)=0, \tag{2.16}$$

where k is the wave number, given by $k=\sqrt{2\mu E/\hbar^2}$, ℓ is the relative angular momentum and $f_\ell(kr)$ are radial-wave functions. The radial wave equations can be solved numerically. At large separation distance r between the projectile and target the nuclear field is negligible and the numerical solutions of $f_\ell(kr)$ are matched to known Coulomb wave functions in order to determine the nuclear phase shifts, δ_ℓ.

The scattering amplitude can be regarded as a summation of Coulomb and nuclear amplitudes [AU78], giving the following:

$$f(\theta_{\text{c.m.}})=f_{\text{C}}(\theta_{\text{c.m.}})+f_{\text{N}}(\theta_{\text{c.m.}}). \tag{2.17}$$

It then follows that the elastic scattering cross-section is given by:

$$\frac{d\sigma}{d\Omega_{\text{c.m.}}}=\left|f(\theta_{\text{c.m.}})\right|^2. \tag{2.18}$$

A partial wave expansion yields the scattering amplitude $f(\theta)$ in terms of δ_ℓ:

$$f(\theta_{\text{c.m.}})=\frac{1}{2ik}\sum_{\ell=0}^{\infty}(2\ell+1)(S_\ell-1)P_\ell(\cos\theta_{\text{c.m.}}), \tag{2.19}$$

$$S_\ell=exp\left(2i(\sigma_\ell+\delta_\ell)\right), \tag{2.20}$$

where S_ℓ is the elastic scattering S-matrix and σ_ℓ are the Coulomb phase shifts. Further simplification gives the scattering cross-section in terms of the reflection coefficients $|\eta_\ell|$ [JA70]:

$$e^{2i(\sigma_\ell+\delta_\ell)}-1=\left(e^{2i\sigma_\ell}-1\right)+e^{2i\sigma_\ell}\left(e^{2i\delta_\ell}-1\right), \tag{2.21a}$$

$$\eta_\ell=e^{2i\delta_\ell}, \tag{2.21b}$$

$$\frac{d\sigma}{d\Omega_{\text{c.m.}}} = \frac{1}{4k^2}\left|\sum_{\ell=0}^{\infty}(2\ell+1)\, i(1-\eta_\ell) P_\ell(\cos\,\theta_{\text{c.m}})\right|^2 . \qquad (2.22)$$

By varying one or more of the six optical potential parameters (V_0, a_{R}, $r_{0\text{R}}$, W_0, a_{I} and $r_{0\text{I}}$) a fit to the elastic-scattering data can be obtained. It should be noted that some ambiguities (the best known is the Igo ambiguity) are associated with such fits [HO78].

2.2.1 Extension of the Optical Model for identical particles

When two identical nuclei collide, the two particles are indistinguishable and the wave function describing the quantum system has to be symmetric or anti-symmetric whether the particles are bosons or fermions, respectively. Exchange of two nuclei in orbital space is equivalent to a transformation $\theta_{\text{c.m.}} \rightarrow \pi - \theta_{\text{c.m.}}$.Thus, the scattering amplitude becomes:

$$f_{\text{s}}(\theta_{\text{c.m.}}) = f(\theta_{\text{c.m.}}) + (-1)^{\text{s}} f(\pi - \theta_{\text{c.m.}}), \qquad (2.23)$$

where $f(\theta_{\text{c.m.}})$ is the amplitude that describes the scattering of distinguishable nuclei. The resulting differential cross-section becomes:

$$\frac{d\sigma}{d\Omega_{\text{c.m.}}} = \sum_{\text{s=0}}^{2\text{I}} \frac{2S+1}{(2I+1)^2}(|f_{\text{s}}(\theta_{\text{c.m.}}|^2), \qquad (2.24)$$

$$= |f(\theta_{\text{c.m.}})|^2 + |f(\pi - \theta_{\text{c.m.}})|^2 + \frac{(-)^{2\text{I}}}{2I+1}((f\theta_{\text{c.m.}}) f^*(\pi - \theta_{\text{c.m.}})$$

$$+ f^*(\theta_{\text{c.m.}}) f(\pi - \theta_{\text{c.m.}})). \qquad (2.25)$$

The third part of Eq. (2.25) is the interference term that depends on spin I as discussed previously in Section 2.1.2 for Mott scattering.

2.3 Distorted Wave Born Approximation (DWBA) for inelastic scattering

When two nuclei collide close to the Coulomb barrier it is possible for one or both of them to be raised to an excited state without loss or gain of nucleons [HO78]. Also, the ions can interact through their Coulomb fields, and this can raise them to excited states. The scattering matrix, proportional to the residual interaction, is sandwiched between the elastic and inelastic channel. In first-order DWBA inelastic scattering is treated as a one-step transition process.

The transitional amplitude [SA80] that describes inelastic scattering from an initial channel (*i*) to a final channel (*f*) is given below:

$$T_{fi}\left(k_f,k_i\right)=\int dr\,\chi_f{}^{(-)^*}\left(k_f,r\right)\left\langle\Phi_f\left|U\left(r,\xi\right)\right|\Phi_i\right\rangle\chi_i^{(+)}\left(k_i,r\right), \tag{2.26}$$

where k_i and k_f are wave numbers of entrance and exit channels, respectively. The distorted waves $\chi_i^{(+)}(k_i,r)$ and $\chi_f{}^{(-)*}(k_f,r)$ describes the relative motion between the colliding nuclei before and after a collision, respectively. The interaction potential, $U\left(r,\xi\right)$, depends on the internal coordinates, ξ, of the excited state. Here, T_{fi} represents the first term in a series expansion involving all possible inelastic channels and thus it is the limit of weak coupling. The interaction may be split into the following component parts:

$$U\left(r,\xi\right)=U_{\mathrm{C}}\left(r,\xi\right)+U_{\mathrm{N}}\left(r,\xi\right), \tag{2.27}$$

where $U_{\mathrm{C}}\left(r,\xi\right)$ is the Coulomb interaction responsible for the Coulomb excitation and $U_{\mathrm{N}}\left(r,\xi\right)$ is the nuclear interaction responsible for excitation via the nuclear field. The Coulomb field is repulsive and the nuclear field attractive, therefore, $U_{\mathrm{C}}\left(r,\xi\right)$ and $U_{\mathrm{N}}\left(r,\xi\right)$ have opposite signs and tend to add destructively resulting in Coulomb-nuclear interference. Finally the inelastic scattering cross-section can be obtained from:

$$\left(\frac{d\sigma}{d\Omega}\right)_{\mathrm{DWBA}} \propto \left|T_{fi}\right|^2 \ . \tag{2.28}$$

Considering a collective model, the nuclear force follows the shape of the nuclear surface. Due to vibrations about a spherical mean of radius R_0, or by rotations of a permanently deformed sphere of radius R_0, the spherically-optical potential is deformed. In DWBA we then expand $U(r)$ as a Taylor series, and neglecting higher-order terms, since only first order DWBA theory is considered.

$$U_{\mathrm{N}}(r,\xi) = U_{\mathrm{N}}(r-R_0) - \delta R \frac{d}{dr} U_{\mathrm{N}}(r-R_0), \tag{2.29}$$

A multipole expansion of the nuclear interaction potential is performed in Eq. (2.29),

$$U_{\mathrm{N}}(r,\xi) = \sum_{LM} U^{\mathrm{N}}_{LM}(r,\xi)\left[i^L Y_{LM}\left(\hat{\mathbf{r}}\right)\right]^*, \tag{2.30}$$

where the coefficients, $U^{\mathrm{N}}_{LM}\left(r,\xi\right)$, are obtained by comparison with the Taylor expansion (Eq. (2.30)). For a 2^L-pole excitation, and applying the Wigner-Eckart theorem and using vibrational or rotational wave-functions, $J_i = 0 \rightarrow J_f = L$. The reduced matrix element for the nuclear interaction is given by:

$$\left\langle J_f = L \left\| U^{\mathrm{N}}_L\left(r,\xi\right) \right\| J_i = 0 \right\rangle \equiv U^{\mathrm{N}}_L\left(r\right) = \delta^{\mathrm{N}}_L \frac{dU_{\mathrm{N}}(r)}{dr}, \tag{2.31}$$

where the nuclear form factor, $U^{\mathrm{N}}_L\left(r\right)$ is evaluated in a similar manner for both vibrational and rotational excitations. The nuclear deformation length is given by:

$$\delta^{\mathrm{N}}_L = \beta^{\mathrm{N}}_{L\mathrm{R,I}} R_{\mathrm{R,I}} \ , \tag{2.32}$$

where the corresponding deformation parameters $\beta^{\mathrm{N}}_{L\mathrm{R}}$ and $\beta^{\mathrm{N}}_{L\mathrm{I}}$ of the optical potential may have different values depending on the geometry of real and imaginary potentials, respectively. The Coulomb form factor $U^{\mathrm{C}}_L(r)$ is evaluated as follows:

$$U_L^{\mathrm{C}}(r) = \frac{3Z_1Z_2e^2}{2L+1}\ \delta_L^{\mathrm{C}} \begin{cases} R_{\mathrm{C}}^{L\text{-}1} / r^{L+1}, & r > R_{\mathrm{C}} \\ r^L / R_{\mathrm{C}}^{L+2}, & r \le R_{\mathrm{C}} \end{cases}. \tag{2.33}$$

The above expression resembles closely that of the nuclear form factor, and the transition amplitude is then obtained in terms of radial wave-functions.

Chapter 3

Experimental details and data extraction

Elastic and inelastic scattering of ^{9}Be + ^{9}Be has been studied using the iThemba LABS (Gauteng) EN tandem Van de Graaff accelerator and associated equipment. This chapter presents a description of the characteristics of the gas-ionisation ΔE-E detector and the heavy-ion scattering measurement. Angular distributions for elastic scattering were measured at E_{Lab} = 9, 12 and 16 MeV. Also, the excitation functions at $\theta_{\mathrm{c.m.}}$ = 90° and 50° were measured from close to the Coulomb barrier in the incident energy range $6 \leq E_{\mathrm{Lab}} \leq 25$ MeV. The present work includes the inelastic scattering cross-sections for ^{9}Be ($5/2^{-}$, 2.430 MeV) at $\theta_{\mathrm{c.m.}} \approx 90°$ and 50° in the same incident energy range of E_{Lab}= 6 - 25 MeV. The second unbound state in ^{9}Be is observed by detecting the recoil ^{9}Be in its ground state. In some instances, a kinematics programme was used in order to determine the position of elastic and inelastic peaks. The experimental technique is outlined briefly below and specific details are given in the following sections. In addition, reviews of inelastic and elastic scattering data (previous and present) are detailed here.

3.1 Beam production and targets

A model 860C sputter ion source from General Ionex Corporation was used to produce negative ^{9}Be ion beams. These were produced by bombarding a positive Caesium-ion onto a cylindrical target cathode. The cathode material consisted of a mixture of high purity ^{9}Be and titanium hydride powder in the ratio 7:3, respectively, which leads to the formation of negative beryllium hydride ion $(^{9}\mathrm{BeH})^{-}$. The mixture was compressed into the oxygen-free copper holder. The momentum of the beam was analysed before being injected into the accelerator. In the gas stripper canal $(^{9}\mathrm{BeH})^{-}$ is stripped to predominantly $^{9}\mathrm{Be}^{3+}$. Typically, a current of 700 nA of $(\mathrm{BeH})^{-}$ could be obtained from the ion source with 10 - 20 nA electrical of $^{9}\mathrm{Be}^{3+}$ delivered to the ^{9}Be target. After acceleration by the tandem accelerator, the beam was focused into the small scattering chamber, at the end of

the C-line where it was scattered by a thin beryllium foil of areal density approximately 50 μg/cm^2.

3.1.1 Inflection magnet scan

The inflection magnet was used in to separate the negative ions extracted from the sputter ion source. An extraction voltage of 24.5 keV was used and a series of negative ions were identified as shown in Fig. 3.1. Although relatively weakly produced, the $(BeH)^-$ component was sufficient to yield a beam current at the target of typically 10 to 20 nA electrical of $^9Be^{3+}$.

3.1.2 Targets

The beryllium target (^{9}Be) was self supporting with an areal density of ~50 μg/cm^2. A thin layer of BaCl acting as the release agent covered the glass microscope slide on which the ^{9}Be vapour was deposited during an E-gun evaporation of ^{9}Be metal. This leads to contamination of the targets with ^{138}Ba. However, a prominent peak in the measured energy spectra due to the Rutherford scattering formula was observed and was used for energy calibration and beam current normalization.

3.2 Experimental set up

The lay-out of the scattering chamber and the nuclear physics C-line is shown in Fig. 3.2. A positive beam ($^9Be^{3+}$ or $^9Be^{4+}$) from the accelerator is guided by the cross-wire on the quartz Faraday cup 1, which allows for the accurate injection into the C-line. The beam is focused down the C-line by the quadrupole magnet into the small scattering chamber. The small scattering chamber has a diameter of 20 cm with a movable top, which can be rotated around the target holder. The movable part is connected to the gas-ionisation via a port carrying the detector collimator. The top part of the small scattering chamber tilts out of the horizontal plane on its

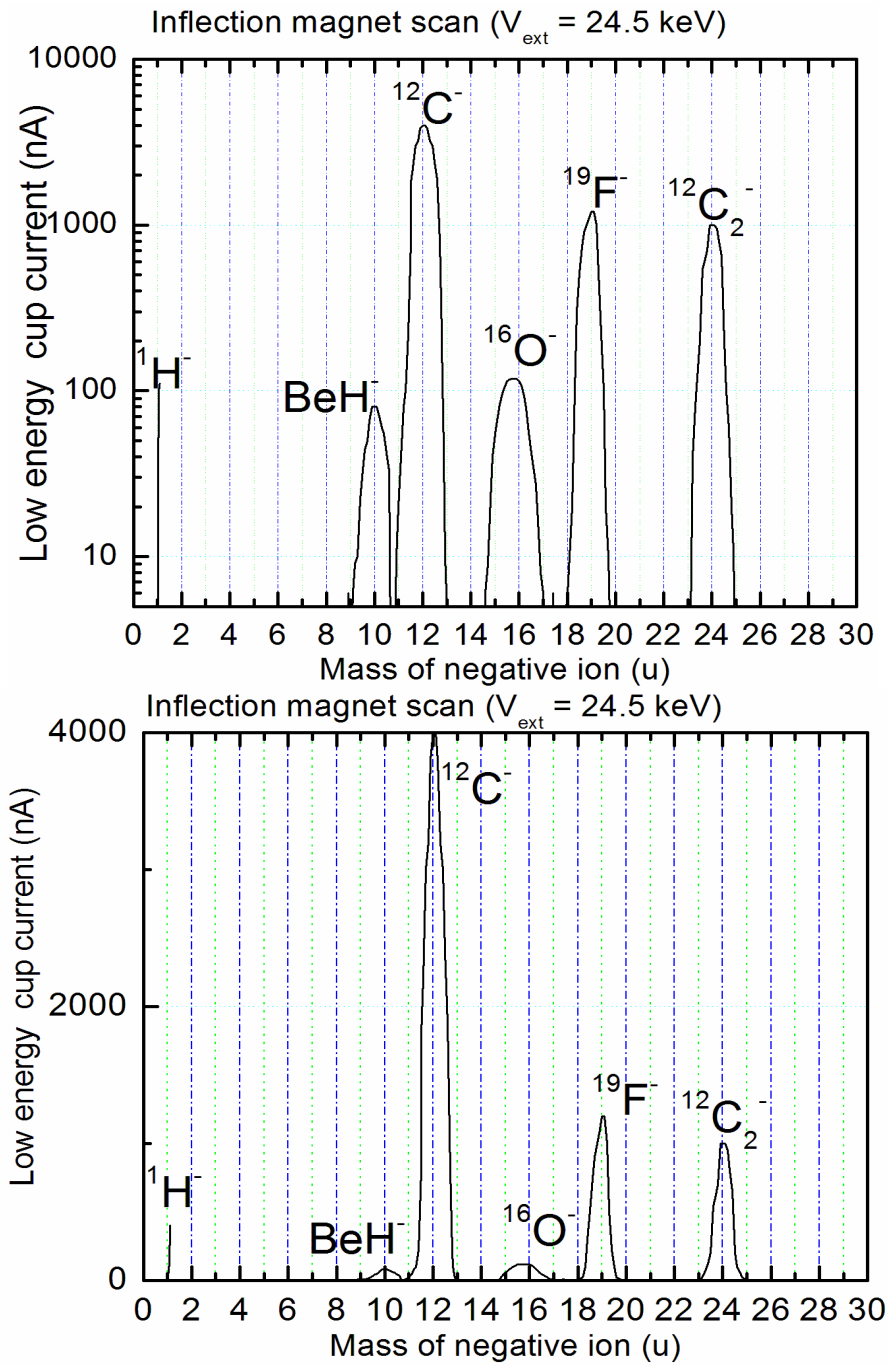


Figure 3.1: Upper: Inflection magnet scan on a log plot of low energy Faraday cup current against mass of a negative ion with source extraction voltage (V_{ext} = 24.5 keV). Lower: inflection magnet scan on a linear plot of low energy Faraday cup current against mass of a negative ion with source extraction voltage (V_{ext} = 24.5 keV).

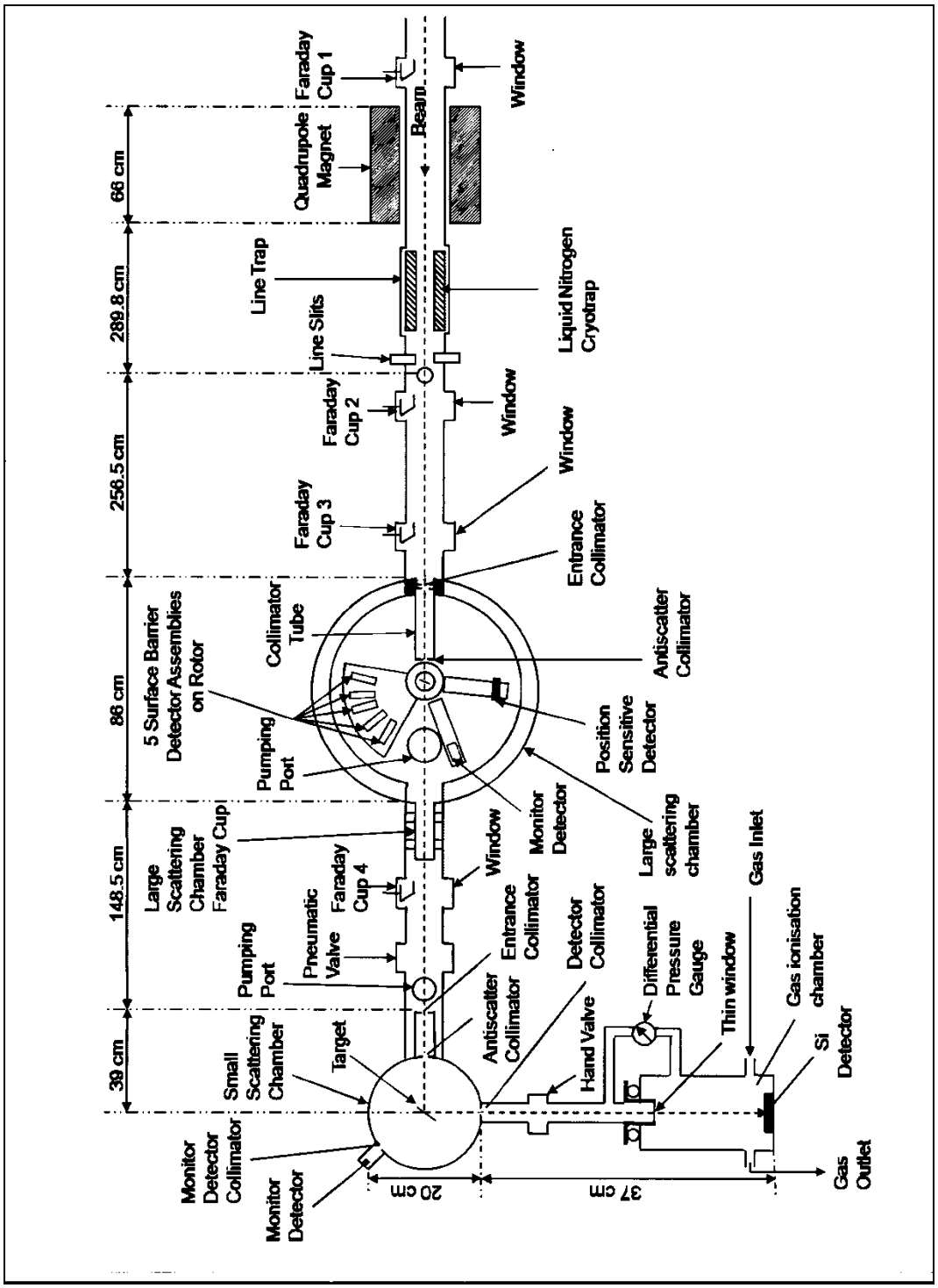


Figure 3.2: The schematic diagram of the C-line and associated equipment at the EN Tandem accelerator of iThemba LABS (Gauteng).

base, allowing measurements to be made on either side of the 0° scattering angle from -20° to 135°.

The horizontal and vertical line slits were adjusted manually defining a rectangular aperture which determined the beam angular divergence at the target (≈ 0.2°). From the beam optics geometry the horizontal acceptance of the detector was 0.6° determined by the 1mm diameter tantalum detector collimator. The target ladder (accommodating up to six targets) was aligned optically to the vertical axis of the chamber. A left-right Rutherford scattering experiment allowed the scattering angle to be determined to ≤ 0.5°.

3.3 Δ*E*-*E* detector

A high resolution gas-ionisation Δ*E*-*E* detector was used to identify the scattered reaction products and determine the corresponding kinetic energies. A diagram of the Δ*E*-*E* gas-ionisation detector is shown in Fig. 3.3. The scattered beryllium ion passes through the gas filled space and comes to rest in the silicon solid-state surface-barrier detector having lost some energy (Δ*E*) due to ionisation in the isobutene gas [WI50].

Using the quantum-mechanical calculation as proposed by Bethe and Bloch, the energy transfer is classified as a measurable quantity (momentum transfer). The Bethe and Bloch equation may be used to describe the energy loss of an ion passing through a medium [LE92]:

$$\frac{dE}{dx} = 2\pi N_A r_e^2 m_e c^2 \rho \frac{Zq^2}{A\beta^2}\left\{\ln\left(\frac{2m_e r^2 v^2 W_{max}}{I^2}\right) - 2\beta^2 - \delta - 2\frac{C}{Z}\right\}, \qquad (3.1)$$

where $2\pi N_A r_e^2 m_e c^2 = 0.1535\ \mathrm{MeVcm^2/g}$,

N_A = Avogadro's constant = 6.022 x 10^{23} mol^{-1},

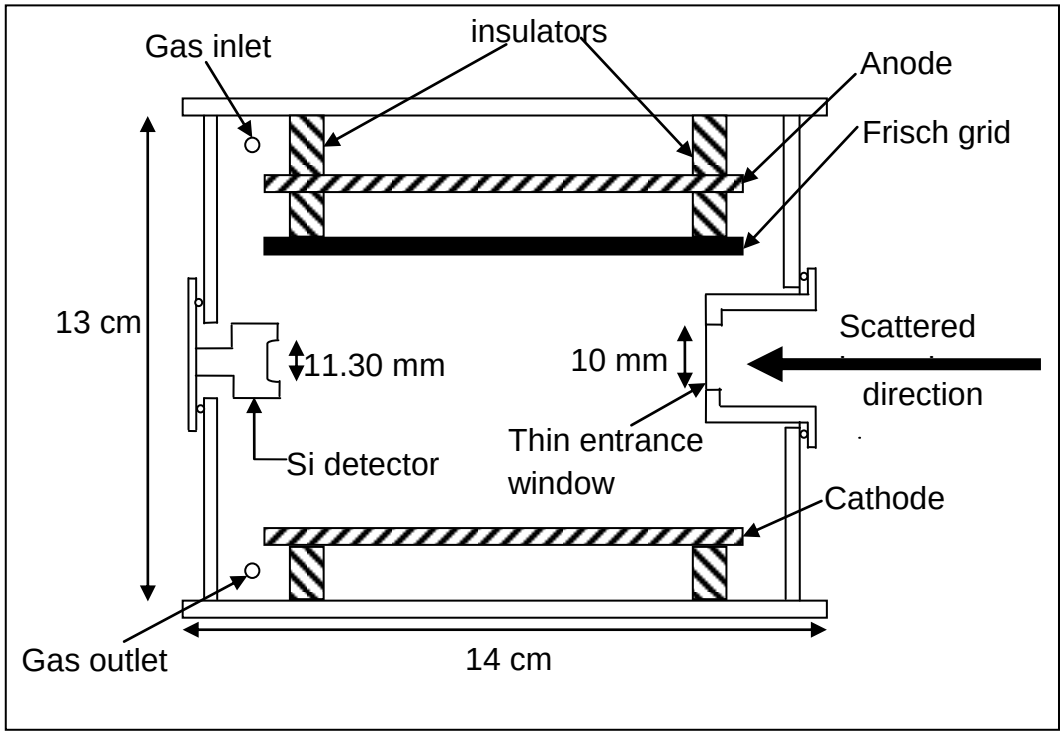


Figure 3.3: Δ*E*-*E* gas-ionisation detector.

r_e = the classical radius of the electron,

m_e = the mass of the electron,

ρ = the density of the absorbing material,

Z = the atomic number of the absorbing material,

q = the charge of the incident particle (electron units),

A = the atomic mass of the absorbing material,

β = the ratio of the velocity of incident particle to that of light (v / c),

W_{max} = the maximum energy transfer in a single collision,

I = mean excitation potential,

δ = the density correction ,

C = the shell conversion,

γ = $(1- \beta^2)^{-1/2}$ and

c = the speed of light.

Considering the energy dependence, at non-relativistic energies, d*E*/d*x* is dominated by the overall 1 - β^2 factor and decreases with increasing velocity. For

non relativistic particles ($v^2 = 2E/m$) with the logarithmic term varying slowly with energy, and neglecting the shell conversion (C) and density correction (δ), Eq. (3.1) reduces to:

$$\frac{dE}{dx} \alpha \frac{mz^2}{E} \quad , \tag{3.2}$$

where m is mass of incident particle (in au).

A particle loses energy ΔE as it travels through the gas and deposits energy E as it is stopped by the Si surface-barrier detector. The product $E\left(dE/dx\right)$ gives a measure of mz^2 which is unique for light isotopes.

The gas–ionisation chamber is not subject to radiation damage, which is quite important in this experiment work since the excited ^{9}Be recoil particles from the target can release neutrons which would destroy a thin ΔE silicon surface barrier-detector [HA89]. The ΔE volume contains iso-butane gas which was set at a steady differential pressure of 1 kPa with respect to the high vacuum scattering chamber. The operating conditions were determined in previous experiments [JI10] and are given in Table 3.1.

Table 3.1 Operating conditions for the ΔE-E gas ionisation detector [JI10].

Iso-butane Differential pressure (kPa)	V_A **(V)**	V_G **(V)**	V_C **(V)**
1	230	30	-30

3.4 Data acquisition system and data extraction

The electronics system connected to the gas-ionisation chamber used in this experiment is shown in Fig. 3.4. The various electronics components were configured and set up as follows. The two signals, ΔE and E_{stop}, from the gas-ionisation chamber and the

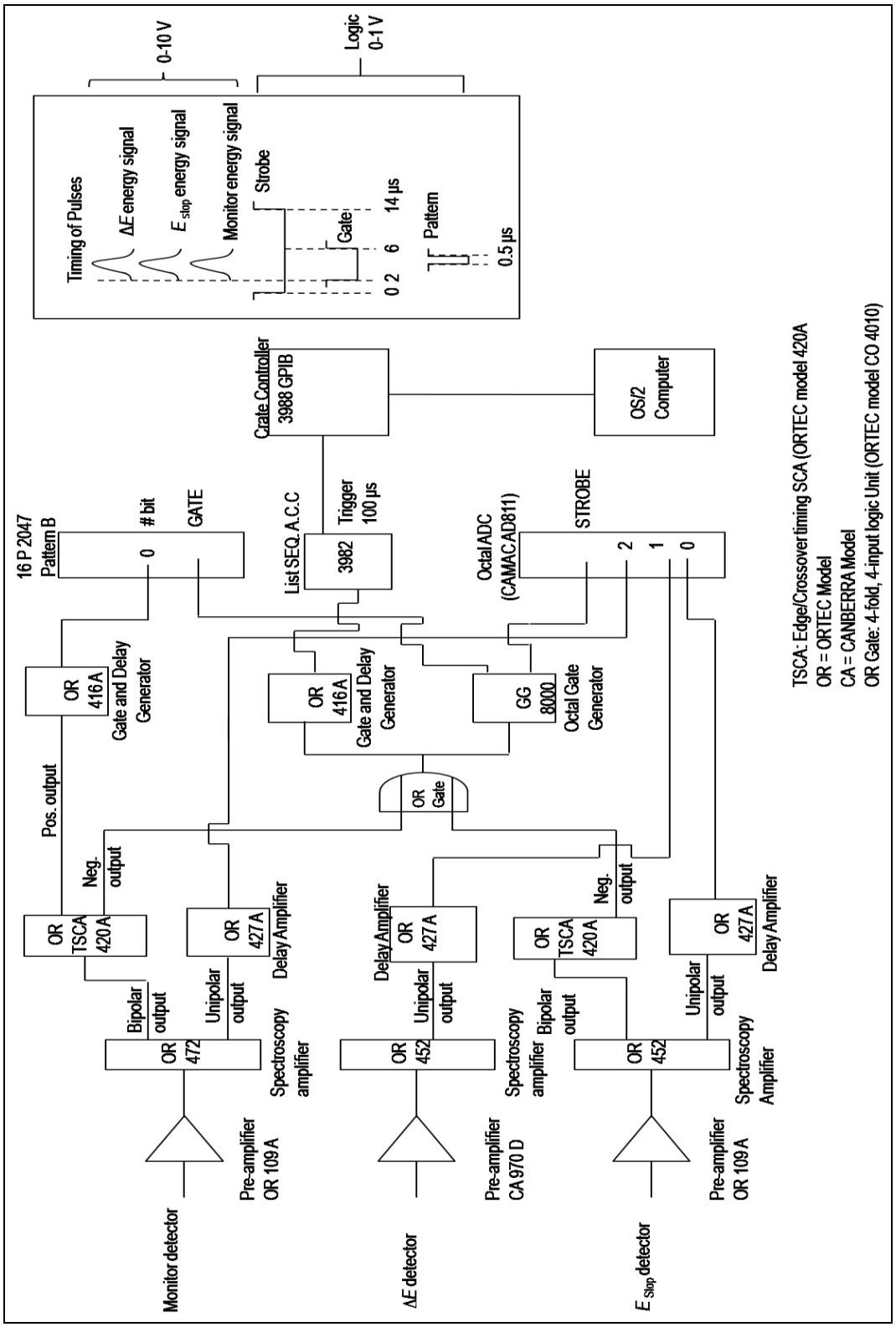


Figure 3.4: Block diagram of the data acquisition system.

monitor detector signal, E_{mon}, were amplified and fed into the ADC unit. The logic part of the circuit distinguished between ΔE-E and monitor detector events. Signals from the CAMAC system were processed by using the WIMPS/2 programme for online data extraction and analysis [FE92]. Scattering data were processed online and pulse height spectra obtained. The signals, ΔE and E_{stop} were plotted against one another. However, the total energy ($E_T = E_{stop} + n\Delta E$) is required and is obtained by normalising at $\theta_{Lab} = 25°$, with and without gas in the ionisation chamber, where n is the normalising factor. The value determined in this experiment was $n = 0.562$.

A typical two dimensional ΔE-E_T spectrum is shown in Fig. 3.5. Here, it can be clearly seen that there is a good separation between low-Z elements. A portion of the ΔE-E_T spectrum corresponding to ^{9}Be maybe projected onto the E_T-axis and the resulting 1-dimensional spectrum is shown in Fig. 3.6. Figure 3.6 (lower) shows an enlarged version, in order to bring out the inelastic scattering ^{9}Be´ peak at $\theta_{Lab} = 25°$. From the 1-dimensional spectra peaks for both elastic and inelastic scattering were identified and fitted using a Gaussian shape fitting procedure with a quadratic background. Given that the quadratic background is defined as follows:

$$B = b_0 + b_1 x + b_2 x^2, \tag{3.3}$$

thus the following formula was used to fit peaks in the measured spectra:

$$y(x) = h \exp\left\{-\frac{1}{2}\left(\frac{x - x_0}{\sigma}\right)^2\right\} + B \ , \tag{3.4}$$

where h is the height of the peak, σ is the standard deviation, x_0 is the peak centroid and x is the channel number.

The area under the Gaussian curve can be obtained from

$$A = h\sigma\sqrt{2\pi} \ , \tag{3.5}$$

WIMPS\ ^{9}Be + ^{9}Be at θ_{Lab} = 25°. 2D

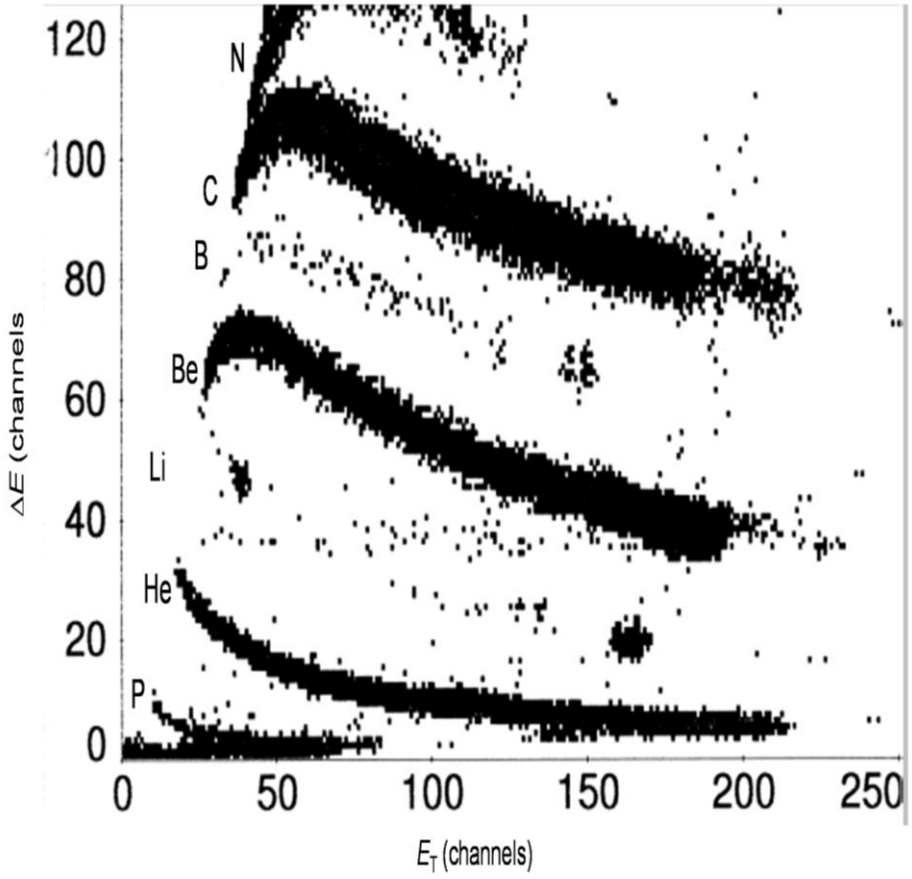


Figure 3.5: Two dimensional ΔE-E_T spectrum for ^{9}Be + ^{9}Be at E_{Lab} = 16 MeV and θ_{Lab} = 25°.

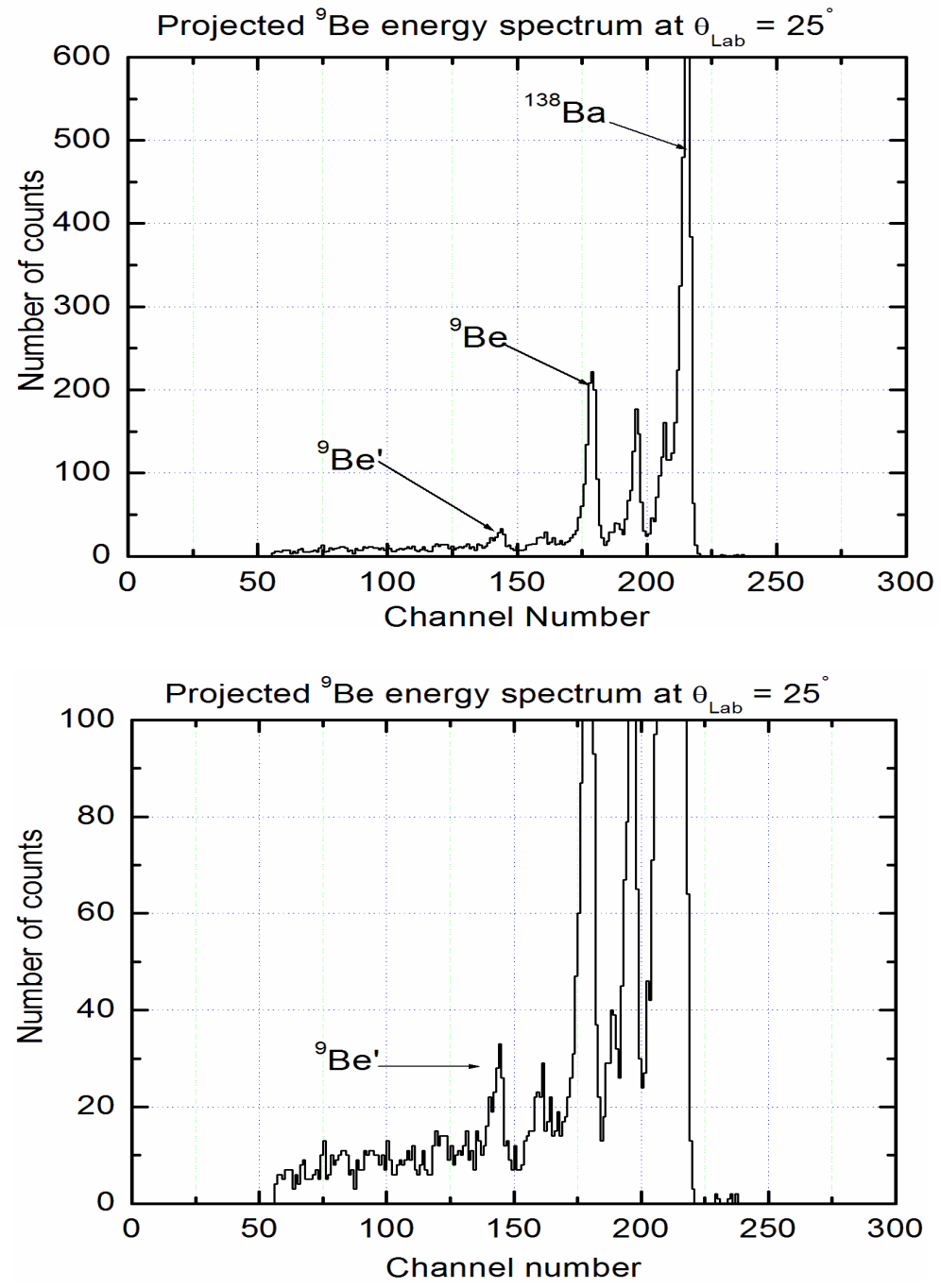


Figure 3.6: One-dimensional spectrum from the ΔE-E_T for ^{9}Be from Fig. 3.5. Upper part: Projected ^{9}Be showing elastic scattering from ^{9}Be and ^{138}Ba. Lower part: Projected ^{9}Be showing more clearly inelastic scattering to the second, unbound excited state ^{9}Be*($5/2^{-}$, 2.43 MeV).

with the total area under the peak being given by

$$P = A + b \ , \tag{3.6}$$

where b is the background under the peak.

The uncertainty ΔA of the extracted peak area was obtained from:

$$\Delta A = \left[\left(P + b \right) \chi^2 \right]^{\frac{1}{2}} \ , \tag{3.7}$$

where χ^2 is the reduced chi-squared and is given by the following:

$$\chi^2 = \frac{1}{N} \sum_i \left[\frac{y_i - y\left(x_i\right)}{\left(\alpha\right)^{\frac{1}{2}}} \right]^2 , \tag{3.8}$$

where N is the number of data points minus the number of variable parameters (degrees of freedom) and α are the uncertainties on the data points y [HA89]. The uncertainties in the extracted peak areas were included as individual errors and were generally in the range 0.5 – 10%.

3.5 Energy resolution of the detector system

The resolution of the gas-ionisation chamber is given in terms of the full width at half maximum of the peak (FWHM) [LE92]. Considering two peaks from the experimental data, they can be resolved if they are separated by a distance greater than their full widths at half maximum width (FWHM).

The total energy resolution of the ΔE-E_T gas-ionisation detector can be determined by several factors that maybe be attributed to:

- Kinematic broadening, ΔE_{kin} is related to the beam divergence at the target and finite angular acceptance of the detector ≈ (200 keV),
- Electronic noise; ΔE_{det} is the contribution from the resolution of the solid state surface-barrier detector and the electronics of the system ≈ 24 keV,
- Energy spread of the incident beam; ΔE_{beam} ≈ 10 keV and

- The energy spread of the energy loss, ΔE_{loss}; is the energy lost by incident particles when interacting with the ^{9}Be target and when passing through the thin window in the gas-ionisation chamber ≈ 110 keV.

The total resolution energy E is given by:

$$\Delta E_{\text{total}} = \left[\left(\Delta E_{\text{kin}}\right)^2 + \left(\Delta E_{\text{det}}\right)^2 + \left(\Delta E_{\text{beam}}\right)^2 + \left(\Delta E_{\text{loss}}\right)^2 \right]^{\frac{1}{2}}, \tag{3.9}$$

resulting in a typical value of $\Delta E_{\text{total}} \approx 230$ keV.

3.6 Determination of scattering cross-sections

Experimentally measured elastic and inelastic cross-sections were obtained as follows:

- The elastic and inelastic scattering yields for angular distributions were obtained from the Gaussian fitting procedure as described in Section 3.4 for each scattering angle and were normalised using the elastic scattering yields from the ^{138}Ba contamination peak in the monitor detector.

- Normalisation for the excitation functions required the Rutherford scattering formula to be applied to the elastic scattering yield from the ^{138}Ba contamination peak seen in the ^{9}Be projected spectrum at each incident beam.

- The normalised centre-of-mass (c.m.) yield was obtained by multiplying the normalised Lab yield by the respective Lab c.m. factors.

$$I\left(\theta_{\text{c.m.}}\right) = I\left(\theta_{\text{Lab}}\right)\left(\frac{\sin^2\theta_{\text{Lab}}}{\sin^2\theta_{\text{c.m.}}}\right)\cos\left(\theta_{\text{c.m.}} - \theta_{\text{Lab}}\right), \tag{3.10}$$

where $I(\theta_{\text{c.m.}})$ is the intensity (yield) at each scattering angle $\theta_{\text{c.m.}}$ in the centre-of-mass reference frame and $I(\theta_{\text{Lab}})$ is the intensity (yield) at each scattering angle in the laboratory frame [MA68].

- Absolute scattering cross-sections were obtained by normalising to the optical model prediction at the most forward scattering angles. Numerical values for the measured cross-sections are given in Tables A1 to A13.

- Finally, the errors quoted in these measurements are calculated from counting statistics of the corresponding peak yields and the error in the ^{9}Be + ^{138}Ba elastic-scattering peak yield.

3.7 Review of elastic and inelastic scattering data

Table 3.2 provides an overview of the data measured. Angular distributions were measured at energies near the Coulomb barrier for elastic scattering of ^{9}Be + ^{9}Be system. The experimental cross-sections divided by the Mott cross-section are shown with errors in Fig. 3.7. Also, measurements of York *et al*. [YO77] were included and are shown together with those of the present work. The dashed line is the result of an optical model calculation and is to guide the eye only. Thus, the data are limited to the angular region $25\,° \leq \theta_{\text{c.m.}} \leq 155°$. The data were normalised to the optical model prediction for ^{9}Be + ^{9}Be system at $\theta_{\text{c.m.}} = 25°$ (discussed later in Chapter 4). This procedure was followed for all the cross-section measurements at the different incident energies. As shown in Fig. 3.7, the $E_{\text{Lab}} = 16$ MeV cross-sections display a strong oscillatory structure that agrees with the previous very limited data measurement done by York *et al*. [YO77]. As the incident energy decrease to E_{Lab} = 12, 9 and 5 MeV the oscillatory structure becomes less pronounced. The 5 MeV data from [YO77] were also included since in the present experimental work scattered ^{9}Be at E_{Lab} = 5 MeV were too low in energy to be measured. The inelastic scattering cross-sections for the particle-unbound state ($5/2^{-}$, 2.430 MeV) of ^{9}Be at E_{lab} = 16 MeV were measured as shown in Fig. 3.8 and were limited to maximum scattering angle $\theta_{\text{c.m.}} \approx 102°$ due to the low energy of the scattered ^{9}Be detected. Two elastic-scattering excitation functions were also measured, namely at $\theta_{\text{c.m.}} = 90°$ and 50°. Here, at $\theta_{\text{c.m.}} = 90°$, the few data points at low incident energies from York *et al*. [YO77] were also included in order to supplement the present work as shown in Fig. 3.9.

Table 3.2 Measured data for ^{9}Be + ^{9}Be scattering at incident energies just above the Coulomb barrier $E_{\mathrm{Lab}}^{\mathrm{CB}}(^{9}\mathrm{Be}+{}^{9}\mathrm{Be}) = 8.0\ \mathrm{MeV}$.

E_{Lab} (MeV)	Reaction Products	θ_{Lab}	$\theta_{\mathrm{c.m}}$
9	^{9}Be ($\frac{3}{2}^{-}$, g.s.) + ^{9}Be ($\frac{3}{2}^{-}$, g.s.)	15°- 45°	30°- 90°
12	^{9}Be ($\frac{3}{2}^{-}$, g.s.) + ^{9}Be ($\frac{3}{2}^{-}$, g.s.)	15°- 45°	30°- 90°
16	^{9}Be ($\frac{3}{2}^{-}$, g.s.) + ^{9}Be ($\frac{3}{2}^{-}$, g.s.) ^{9}Be´ ($\frac{3}{2}^{-}$, g.s.) + ^{9}Be* ($\frac{5}{2}^{-}$, 2.430MeV)	12.5°- 45° 12.5°- 45°	25°- 90° 33°- 116°
6 - 25	^{9}Be ($\frac{3}{2}^{-}$, g.s.) + ^{9}Be ($\frac{3}{2}^{-}$, g.s.)	25°	50°
6 - 25	^{9}Be´ ($\frac{3}{2}^{-}$, g.s.) + ^{9}Be* ($\frac{5}{2}^{-}$, 2.430 MeV)	25°	≈ 50°
7 - 24	^{9}Be ($\frac{3}{2}^{-}$, g.s.) + ^{9}Be ($\frac{3}{2}^{-}$, g.s.)	45°	90°
7 - 24	^{9}Be´ ($\frac{3}{2}^{-}$, g.s.) + ^{9}Be* ($\frac{5}{2}^{-}$, 2.430 MeV)	45°	≈ 90°

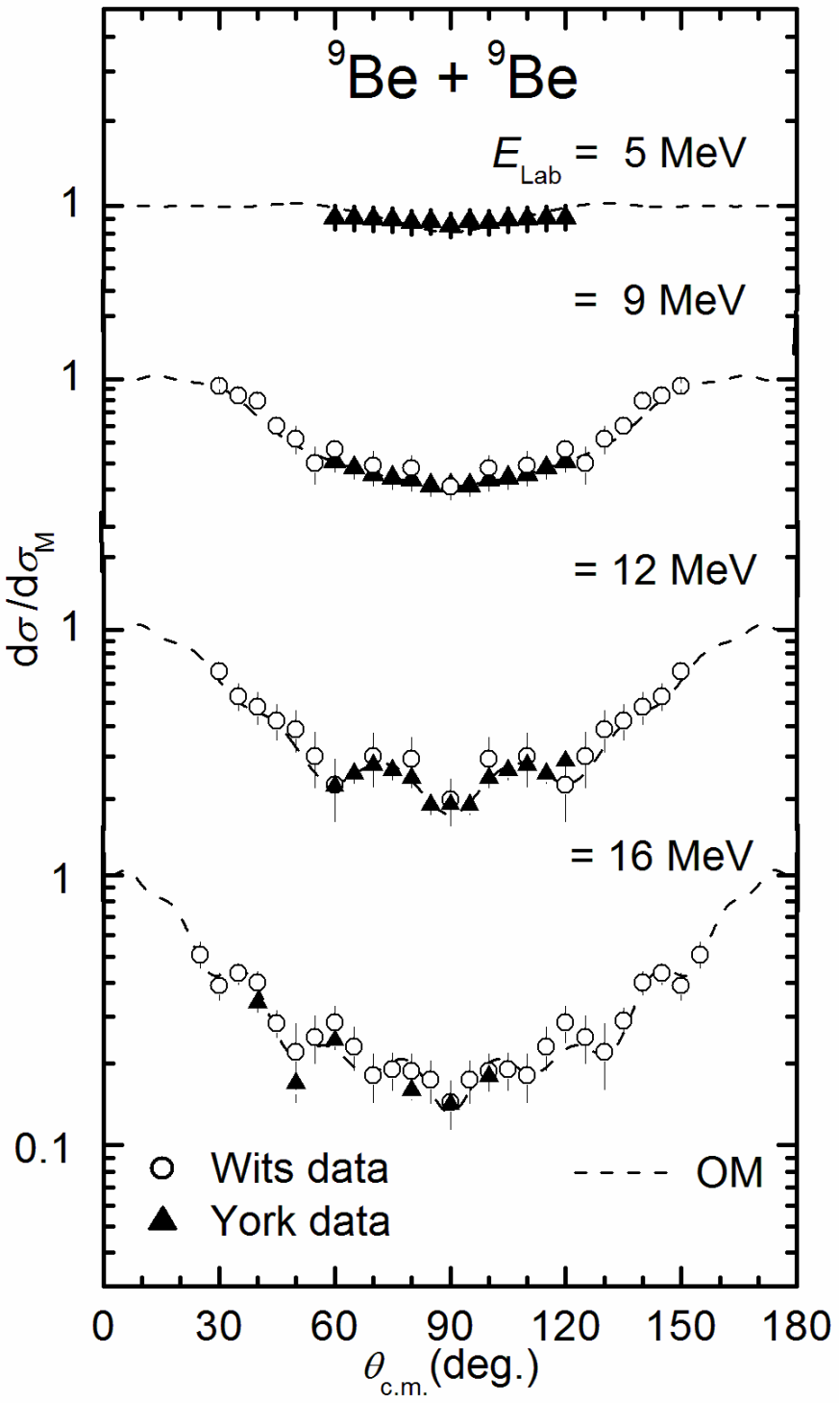


Figure 3.7: Angular distributions for the elastic scattering of ^{9}Be + ^{9}Be at E_{Lab} = 5, 9, 12 and 16 MeV including data from York [YO77]. Note that the above dashed line is to guide the eye and represents an Optical Model (OM) calculation.

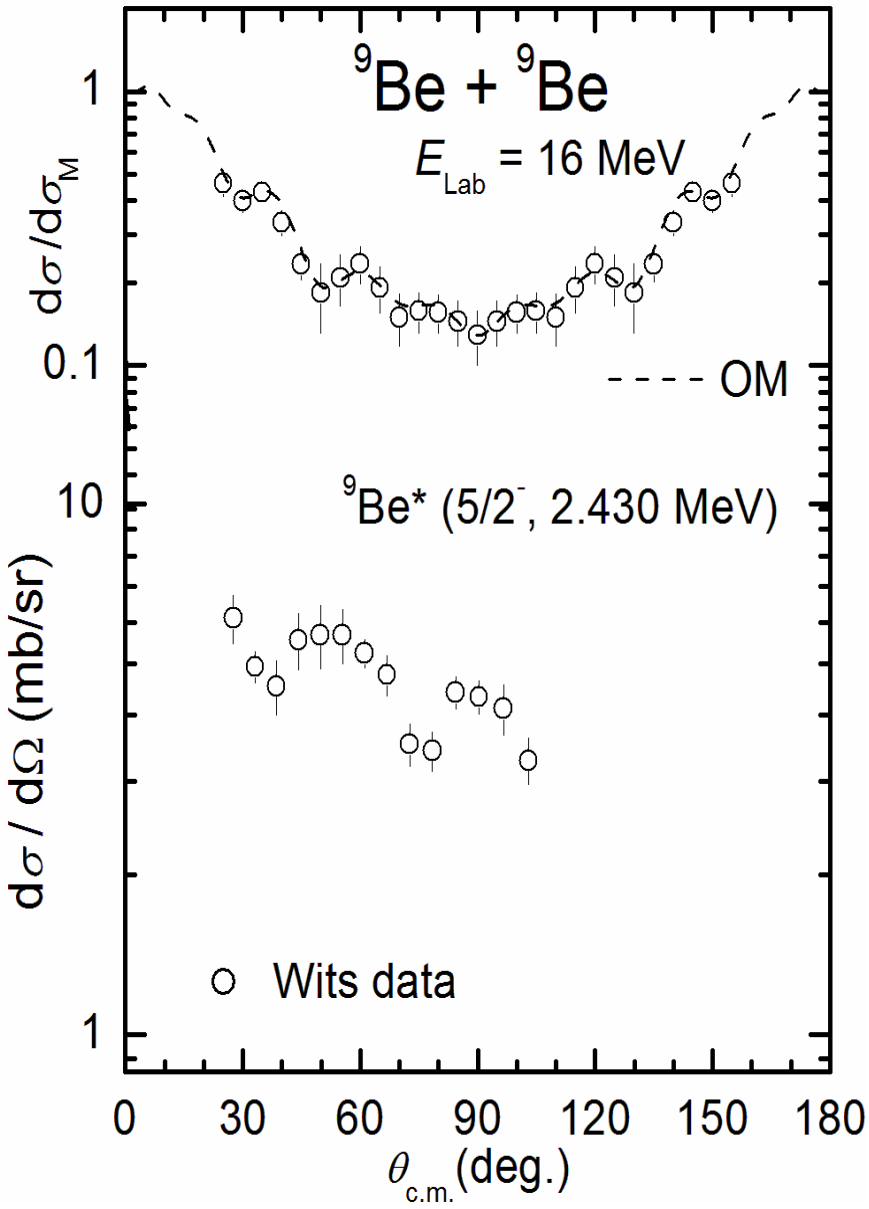


Figure 3.8: Upper part: Angular distribution for the elastic scattering of ^{9}Be + ^{9}Be at E_{Lab} = 16 MeV.

Lower part: Inelastic excitation of the second, unbound, state in ^{9}Be*(5/2$^-$, 2.430 MeV) .

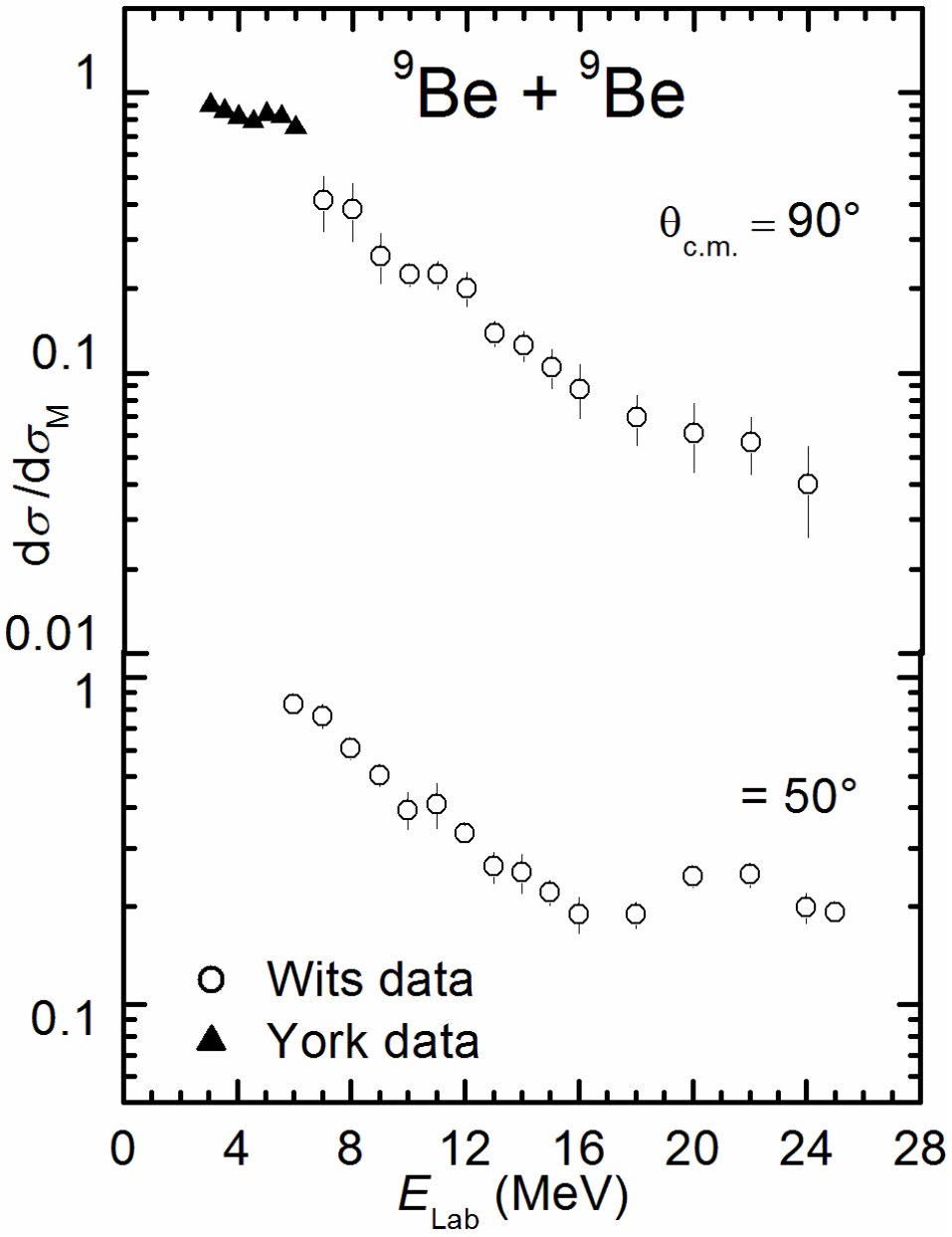


Figure 3.9: Upper part: Excitation function for the elastic scattering of ^{9}Be + ^{9}Be at $\theta_{c.m.}$ = 90° expressed as the ratio of the measured cross-section to Mott cross-section for E_{Lab} = 7 to 24 MeV including data from York *et al*. [YO77].
Lower part: Excitation function for the elastic scattering of ^{9}Be + ^{9}Be at $\theta_{c.m.}$ = 50° expressed as the ratio of the measured cross-section to the Mott cross-section for E_{Lab} = 7 to 25 MeV.

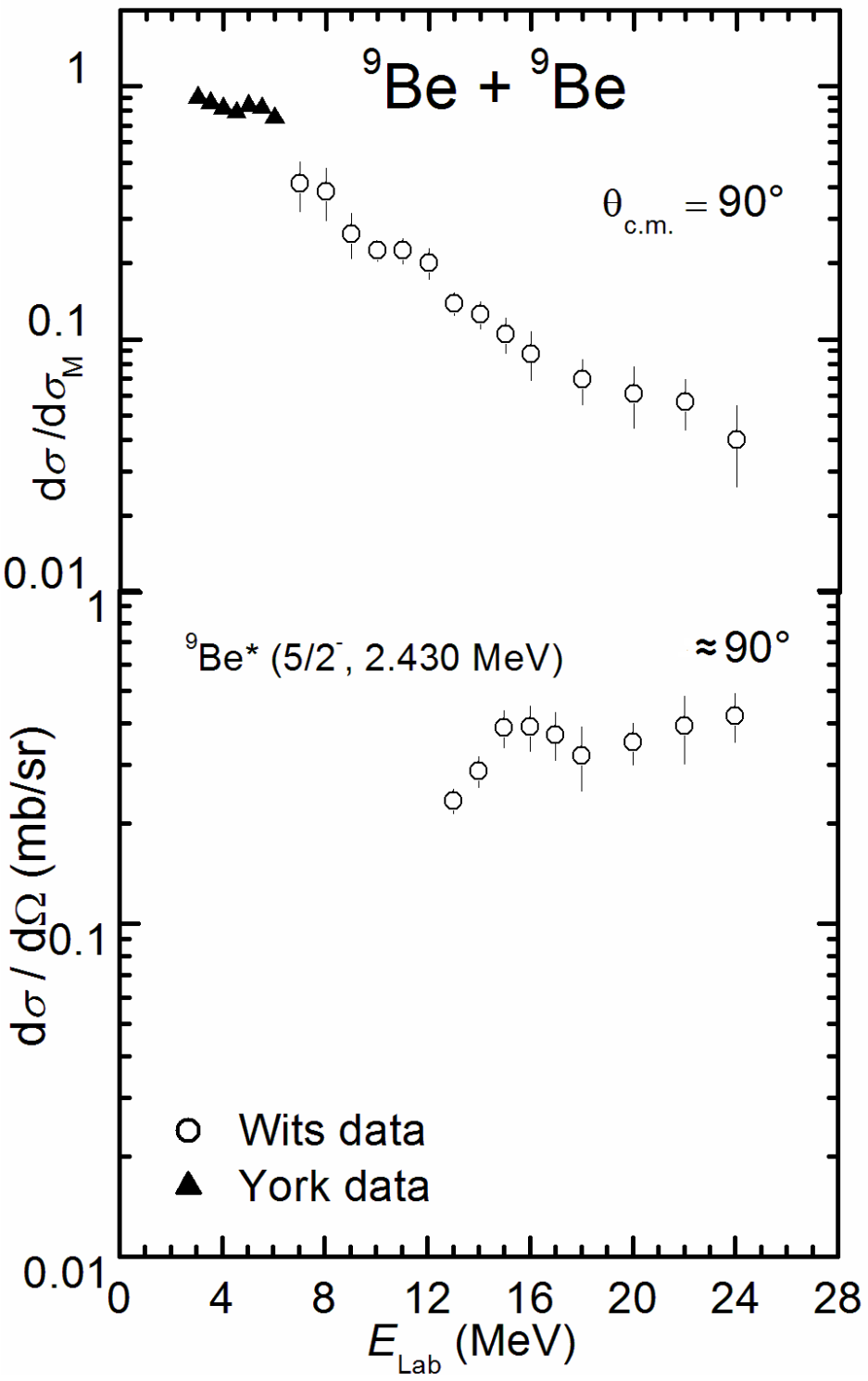


Figure 3.10: Upper part: Excitation function for the elastic scattering of ^{9}Be + ^{9}Be at $\theta_{c.m.}$ = 90° at E_{Lab} = 7 to 24 MeV including data from York *et al*. [YO77].
Lower part: Inelastic-scattering excitation function of ^{9}Be + ^{9}Be at $\theta_{c.m.} \approx 90°$.

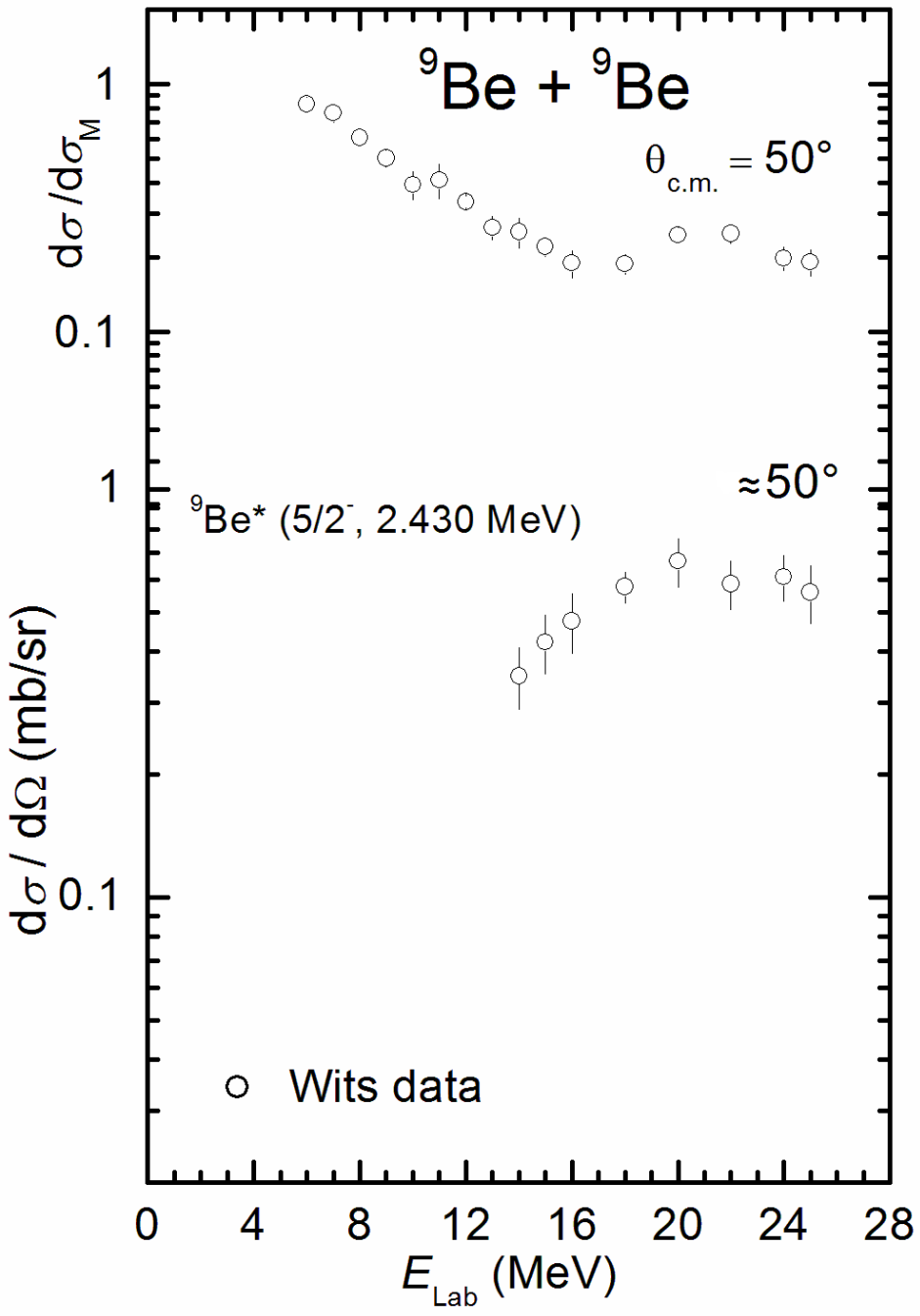


Figure 3.11: Upper part: Excitation function for the elastic scattering of ^{9}Be + ^{9}Be at $\theta_{c.m.}$ = 50° at E_{Lab} = 7 to 24 MeV.

Lower part: Inelastic-scattering excitation function of ^{9}Be + ^{9}Be at $\theta_{c.m.} \approx 50°$.

As can be seen, the ^{9}Be + ^{9}Be excitation function data exhibit a smooth behaviour with small oscillations which become more pronounced as the incident energy increases. Inelastic scattering data for the excited state ^{9}Be*(5/2^{-}, 2.43 MeV) were obtained for the excitation functions at $\theta_{\text{c.m.}} \approx 90°$and 50° are shown in Figs. 3.10 and 3.11. The inelastic scattering cross-sections rise sharply at the Coulomb barrier ($E_{\text{Lab}}^{\text{CB}} = 8.0$ MeV) and reach a plateau at about E_{Lab} = 16 MeV.

Chapter 4

Analysis and discussion

4.1 Introduction

The present elastic scattering results are analysed together with data found in the literature [YO77] and the effect of intrinsic spin on the interference term of Mott scattering is investigated. Subsequently, inelastic scattering data are analysed within the DWBA using the optical potential determined previously from fits to the elastic-scattering data.

4.2 Effect on intrinsic spin on identical particle systems

The Mott scattering formula given by Eq. (2.5) is used for the description of the Coulomb scattering. The third part of Eq. (2.5) is the interference term which depends on the intrinsic spin or angular momentum of the ground spin state, *I*. As illustrated in Fig. 4.1, the Mott scattering cross-sections for the ^{9}Be + ^{9}Be system get shallower as spin *I* increases and the relative change in cross-section becomes less marked as expected from the denominator of the interference term of Eq. (2.5). It should be noted that elastic scattering of identical particles yields angular distributions that exhibit symmetry around $\theta_{\text{c.m.}} = 90°$ [SA80] and, as such, is also a consequence of the quantum statistics of identical particles.

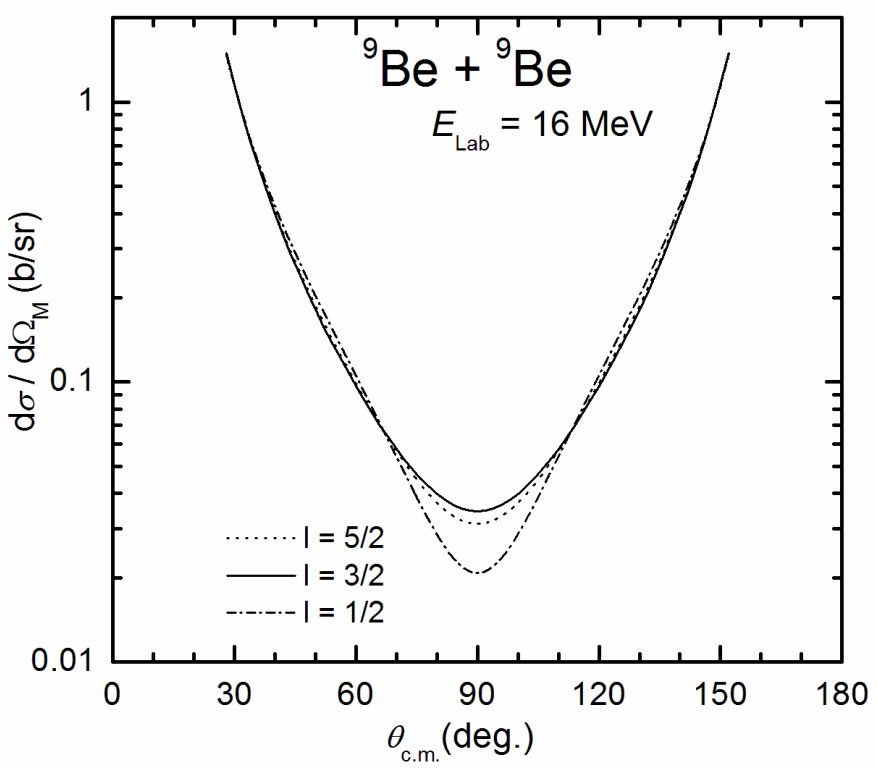


Figure 4.1: Angular distributions for elastic scattering of ^{9}Be + ^{9}Be at E_{Lab} = 16 MeV showing the influence of different intrinsic spin values, I, on the Mott scattering cross-section, where I = 1/2, 3/2 and 5/2, noting that ^{9}Be has a ground state intrinsic spin value of I = 3/2.

4.3 Optical model analysis of elastic scattering

The experimentally measured elastic scattering angular-distributions and excitation functions for ^{9}Be + ^{9}Be were analysed in terms of the Optical Model (OM) for the elastic scattering. This was performed using a modified version of the computer code A-THREE [AU78]. Extensive use was made of the search routine of A-THREE in order to determine the optical potentials for the best fits to the angular distribution data. When searching using the A-THREE search routine the aim was to minimise the mean square deviation, χ^2, between the experimental and theoretical results and is defined as [PO76]:

$$\chi^2 = \frac{1}{N}\sum_{L=1,N}\left(\frac{D_i - F_i}{\varepsilon_i}\right)^2 , \qquad (4.1)$$

where D_i are the data points, F_i are the corresponding calculated fits, ε_i are the errors in the data points and N is the total number of data points. For consistency, the results found by York *et al*. [YO77] for their C-1 optical potential were checked using the published data at E_{Lab} = 5, 9, 12 and 16 MeV and were reproduced. Here, a value for the Coulomb radius was taken from the electron scattering, R_C = 3.23 fm [SA80].

In the present analysis only the data of York *et al*. [YO77] at E_{Lab} = 5 MeV were used (not measurable using the present experimental set-up) together with the newly measured, more extensive, angular distributions at E_{Lab} = 9, 12 and 16 MeV. Values for the optical model parameters determined during various fits are given in Table 4.1. So that valid comparisons can be made, the geometry used by York *et al*. [YO77] was not varied ($R_{OR} = R_{OI}$ = 1 fm and $a_R = a_I$ = 0.632 fm). This meant that the real and imaginary potential well depths were varied (V_0 and W_1, respectively), The imaginary part of the nuclear potential, which was given by the derivative of the real potential form factor, was described by a well depth W_1 and for more final fits the absolute normalisation of the measured data was varied using a scaling parameter (see Table 4.1). The various optical potential parameter sets used or determined are referred to as C-1, W-1, W-2, W-3, and W-4 and are detailed below. For the sake of intercomparison, Figs 4.2, 4.3, 4.4, and 4.5 follow directly after Table 4.1.

4.3.1 Parameter set C-1 and W-1

The optical potential parameter set C-1 obtained by York *et al*. [YO77] was used as a starting point for the present analysis, the results of which are given by the dashed lines in Fig. 4.2. However, it should be noted that the value obtained for W_1 at E_{Lab} = 16 MeV was an extrapolation from the corresponding values E_{Lab} = 9 and 12 MeV due to the poor quality of data as measured by York *et al*. [YO77]. Bearing this in mind, a search was done on W_1 using the present superior data at E_{Lab} = 16 MeV which resulted in a much lower value of χ^2 (see set W-1 of Table 4.1) while reducing somewhat, the value of W_1. The results of W-1 are shown as a solid line in Fig. 4.2.

4.3.2 Parameter set W-2

The next step in the analysis was to determine if better fits to the data could be made by varying both V_0 and W_1. This resulted in parameter set W-2 where it can be seen in Table 4.1 that significantly smaller values of χ^2 were obtained. The corresponding fits are shown as the solid lines in Fig. 4.3.

4.3.3 Parameter set W-3

Measured absolute elastic scattering cross-sections when normalised to Coulomb scattering at small scattering angles generally have an accuracy of $\pm 15\%$. Therefore, using parameter set W-2 as the starting point, V_0 and W_1 were again allowed to vary together with an overall scaling factor for each set of data at E_{Lab} = 5, 9, 12 and 16 MeV. This resulted in lower values for χ^2 and normalisation of the data between 3% and 12% while not affecting significantly the values V_0 and W_1 (see parameter set W-3 of Table 4.1). The results of the fit using set W-3 are shown as the solid lines in Fig. 4.4.

4.3.4 Parameter set W-4 and elastic scattering excitation functions

It can be expected that over the relatively small incident energy range of E_{Lab} = 5 to 16 MeV, an energy–dependent potential is not required. Therefore, as a starting point for determining an energy-independent optical potential, the average of the values for V_0 and W_1 found in W-3 were used and were allowed to vary while simultaneously fitting for the data at E_{Lab} = 5, 9, 12 and 16 MeV. This resulted in only slightly higher values of χ^2 producing parameter set W-4 of Table 4.1 the results for which are shown as the solid lines in Fig. 4.5. It now becomes a straight forward matter to apply the resulting energy-independent optical potential set W-4 to the measured ^{9}Be + ^{9}Be excitation functions. The data and the corresponding optical model fits (solid lines) are displayed in Fig. 4.6 for $\theta_{\mathrm{c.m.}}$ = 50° and 90°.

Table 4.1: Optical Model parameter searching

Set	E_{Lab} **(MeV)**	V_0 **(MeV)**	W_1 **(MeV)**	χ^2	**normalisation**
C-1	5	189.30	6.6	7.65	
	9		22.2	21.61	
	12		33.9	10.03	
	16		49.60	17.98	
W-1	16	189.3	45.57	3.30	
W-2	5	204.9	7.8	2.55	
	9	157.08	24.08	13.11	
	12	113.97	28.91	1.01	
	16	175.06	43.72	2.43	
W-3	5	211.52	6.7	1.47	0.952
	9	160.56	18.71	10.15	0.974
	12	117.41	26.61	0.75	0.969
	16	178.44	38.67	1.41	0.879
W-4	5	155.09	34.12	1.55	0.952
	9			11.96	0.974
	12			1.94	0.969
	16			1.95	0.879

C-1- York potential [YO77]

W-1 - searching on W_1 keeping V_0 constant

W-2 - searching on varying both V_0 and W_1

W-3 - searching varying both V_0 and W_1 scaling

W-4 - searching V_0, W_1 and on 3 energies fixed scaling

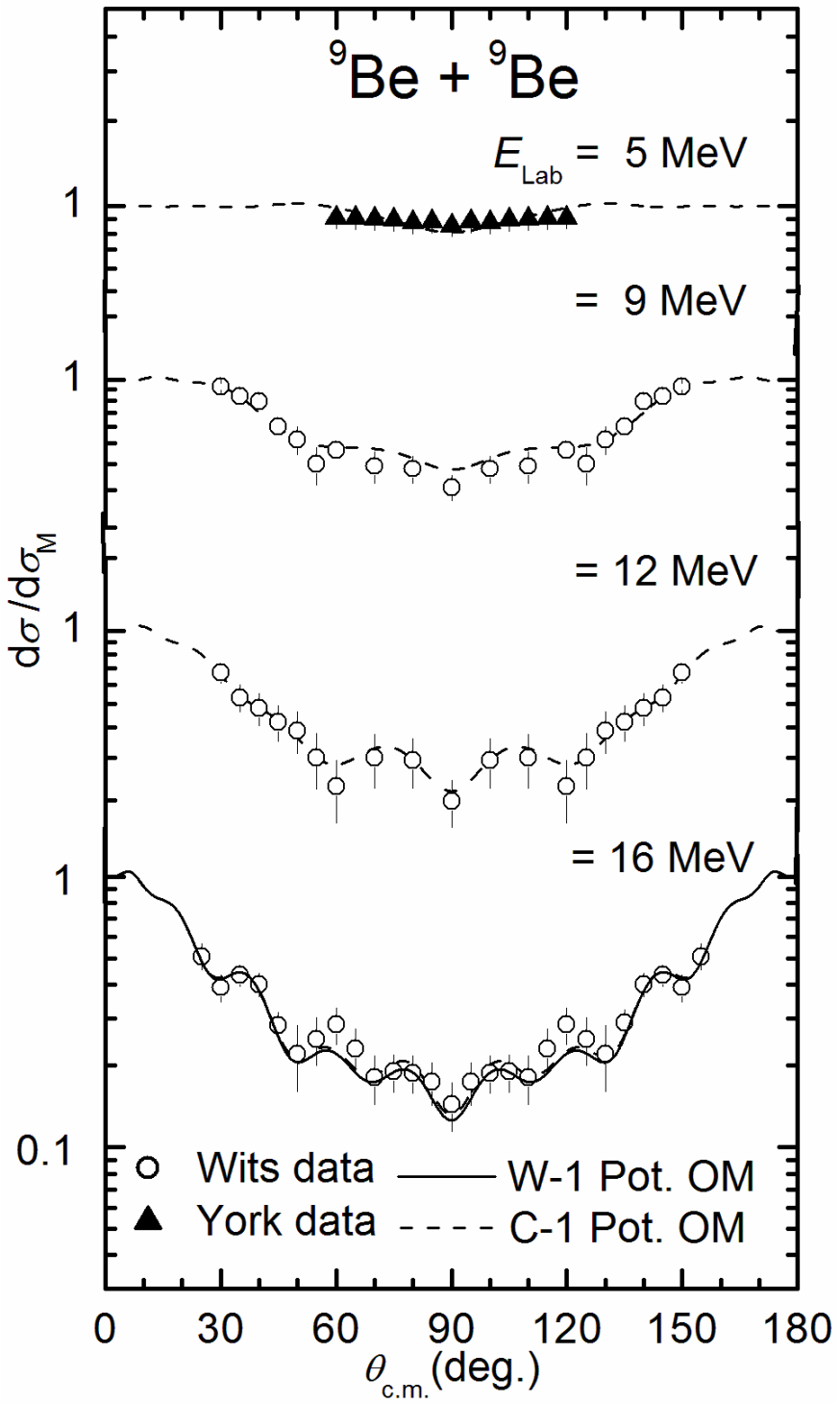


Figure 4.2: Angular distributions for the elastic scattering of ^{9}Be + ^{9}Be at E_{Lab} =5, 9, 12 and 16 MeV using the C-1 and W-1 potentials.

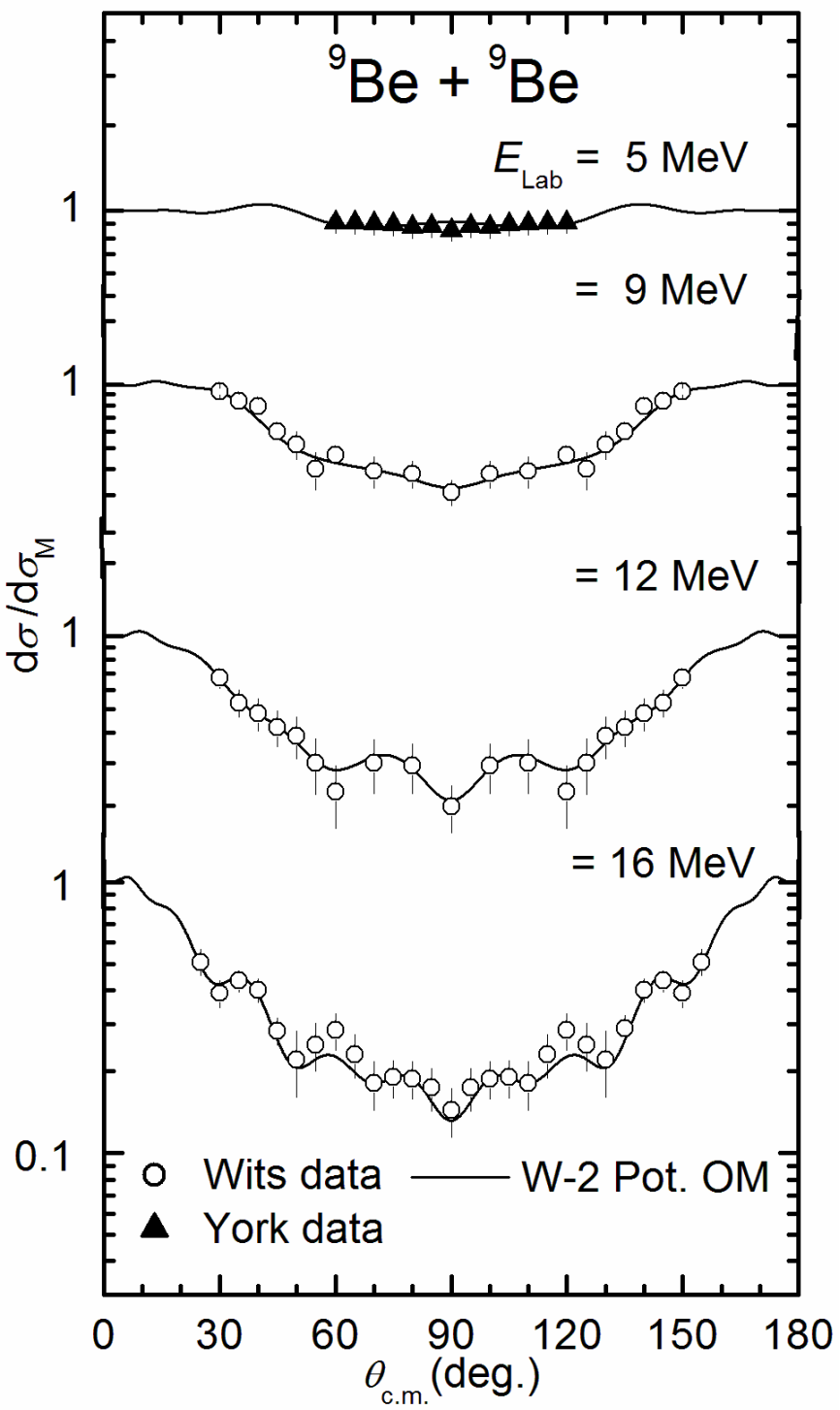


Figure 4.3: Angular distributions for the elastic scattering of ^{9}Be + ^{9}Be at E_{Lab} = 5, 9, 12 and 16 MeV using the W-2 Potential

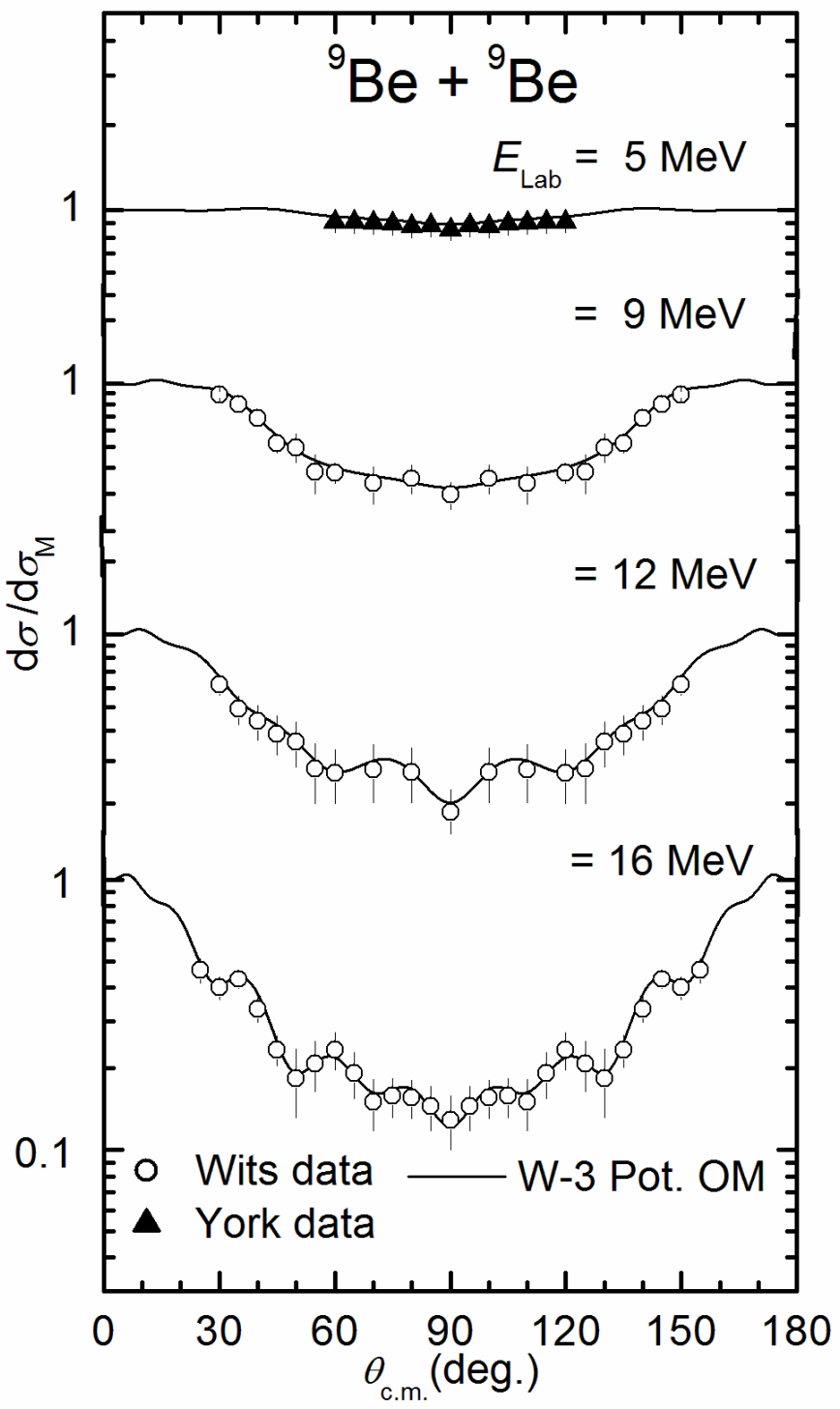


Figure 4.4: Angular distributions for the elastic scattering of ^{9}Be + ^{9}Be at E_{Lab} =5, 9, 12 and 16 MeV using the W-3 potential.

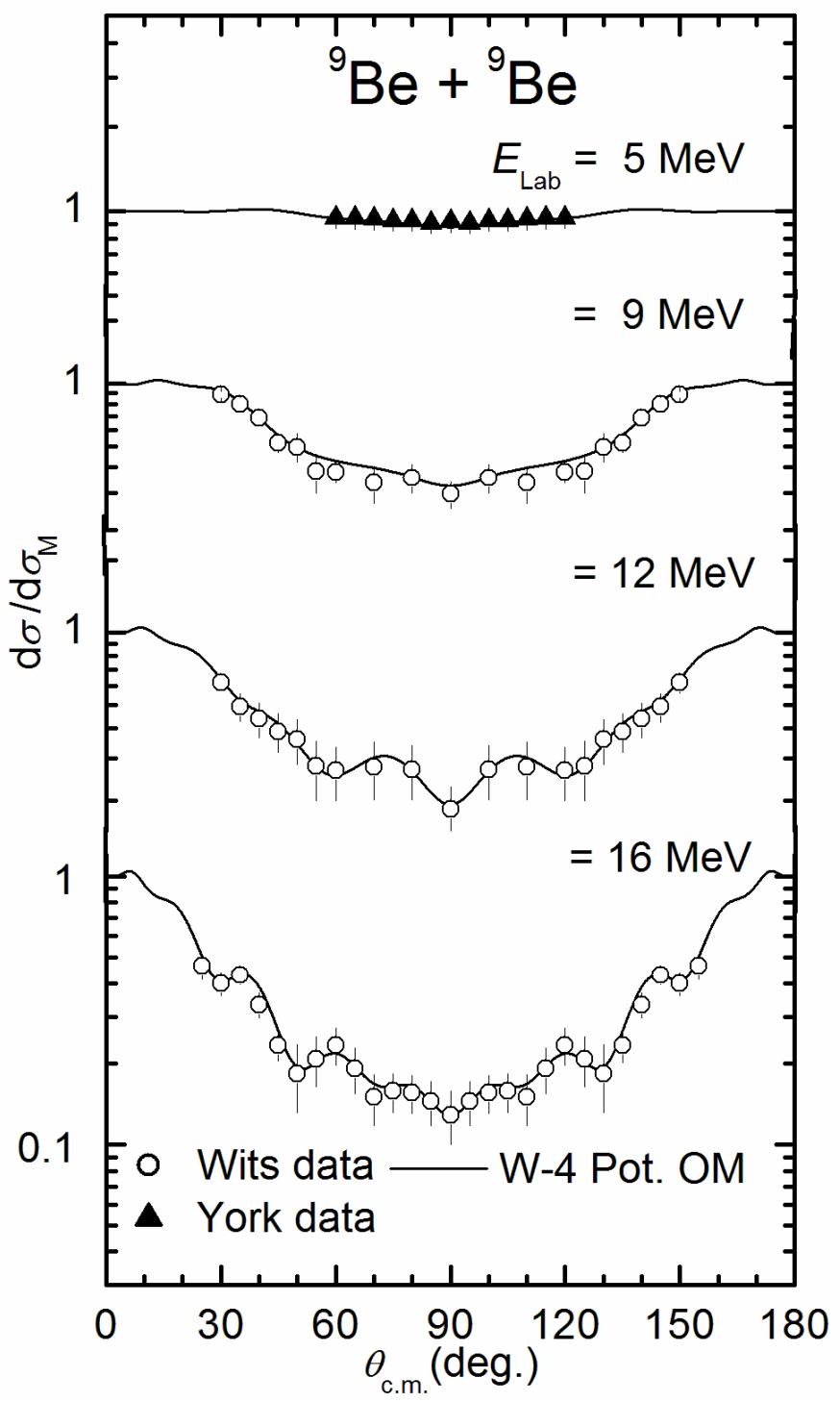


Figure 4.5: Angular distributions for the elastic scattering of ^{9}Be + ^{9}Be at E_{Lab} = 5, 9, 12 and 16 MeV using the W-4 potential.

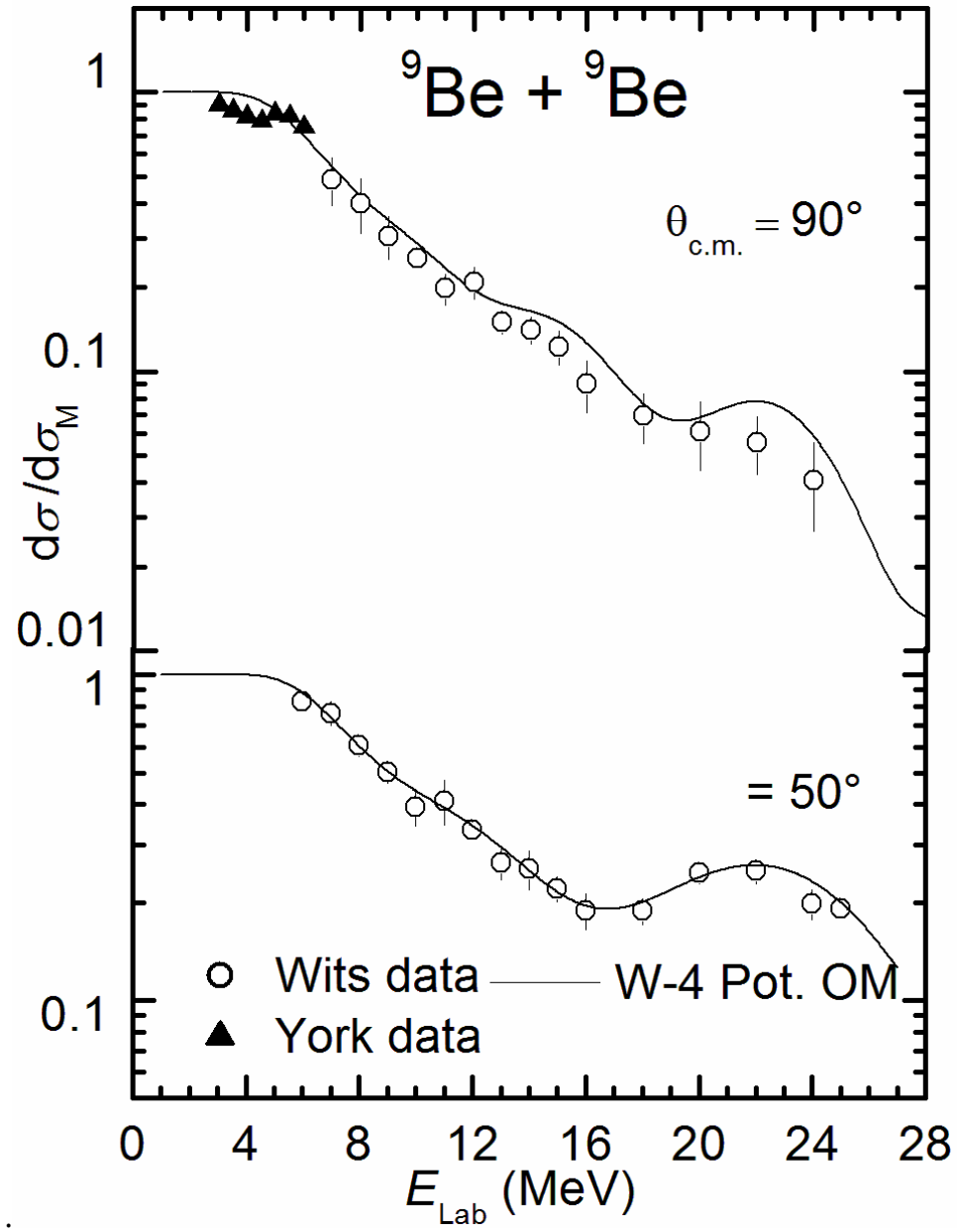


Figure 4.6: Upper part: Excitation function for the elastic scattering of ^{9}Be + ^{9}Be at $\theta_{c.m.}$ = 90° expressed as the ratio of the measured cross-section to Mott cross-section for E_{Lab} = 7 to 24 MeV including data from York *et al*. [YO77].

Lower part: Excitation function for the elastic scattering of ^{9}Be + ^{9}Be at $\theta_{c.m.}$ = 50° expressed as the ratio of the measured cross-section to Mott cross-section for E_{Lab} = 7 to 25 MeV.

4.4 DWBA analysis for inelastic scattering to $^{9}Be^{*}(5/2^{-}, 2.430\ MeV)$

The Distorted Wave Born Approximation (DWBA) analysis technique has been outlined in Section 2.3. Calculations were performed for inelastic scattering to the second, unbound, $^{9}Be^{*}(5/2^{-}, 2.430$ MeV) using the computer code DWIS [VI73], a modified version of the DWUCK by P. D. Kunz. Here, long range Coulomb excitation is properly taken into account by allowing for 400 partial waves and integration of the radial wave functions to 75 fm. Results for the angular distributions measured at E_{Lab} = 16 MeV are shown in Fig. 4.7. A fit to the elastic scattering data (scales as the deformation parameter squared) was obtained by varying the deformation parameters β_2^{C} and β_2^{N} while requiring that the Coulomb and nuclear deformation lengths be equal i.e. $\delta_2^{\mathrm{C}} = \delta_2^{\mathrm{N}}$ with $\delta_2^{\mathrm{C}} = \beta_2^{\mathrm{C}} R_{\mathrm{C}}$ and $\delta_2^{\mathrm{N}} = \beta_2^{\mathrm{N}} R_{\mathrm{R}}$. The derivative form factor came from only the real nuclear potential since the imaginary part did not make a significant contribution. The same optical potential parameters and extracted deformation lengths as found in the fit to angular distributions at E_{Lab} = 16 MeV were used for calculating the excitation functions taken at $\theta_{\mathrm{c.m.}} \approx 50°$and 90° where the results are displayed correspondingly in Figs. 4.8 and 4.9.

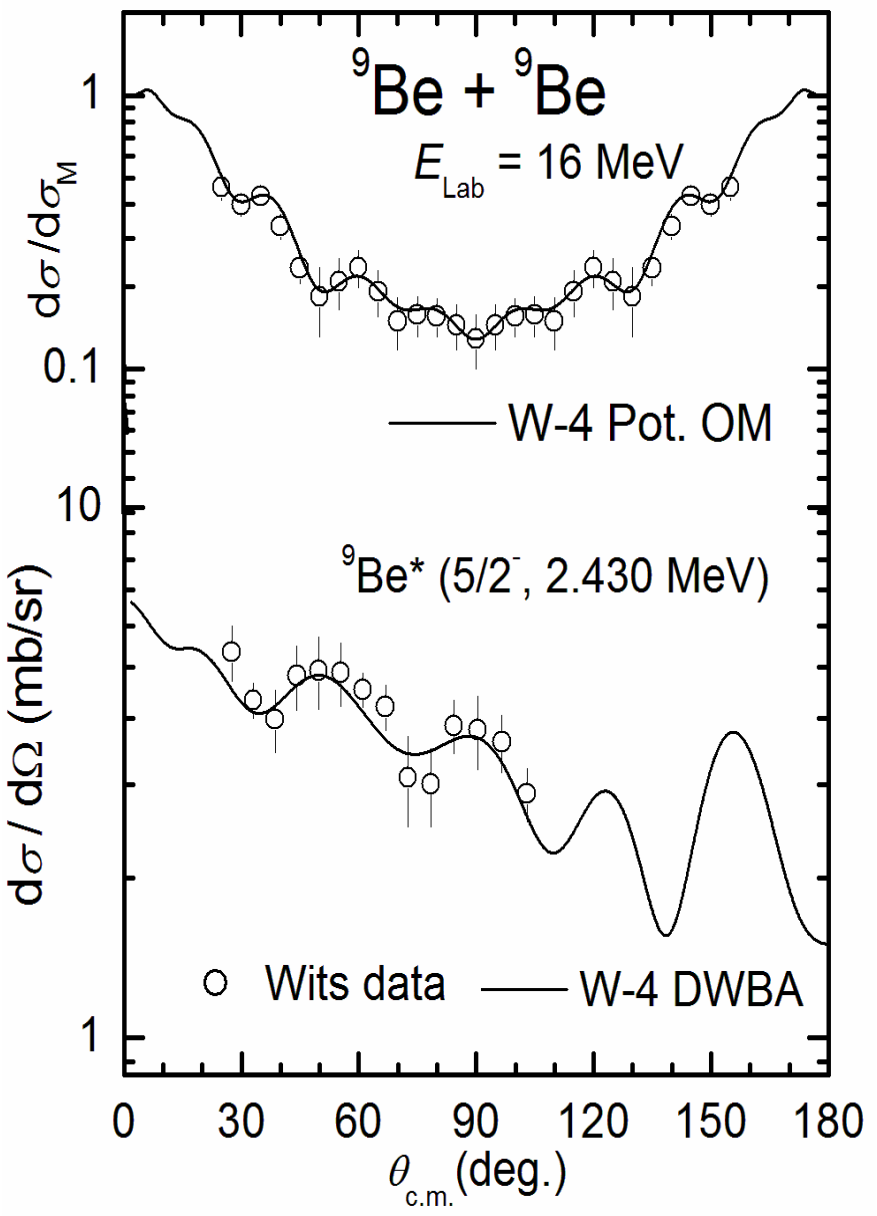


Figure 4.7: Upper part: Angular distributions for the elastic scattering of ^{9}Be + ^{9}Be at E_{Lab} = 16 MeV. Lower part: Inelastic excitation of the second unbound state in ^{9}Be (5/2$^-$, 2.430 MeV at E_{Lab} = 16 MeV.

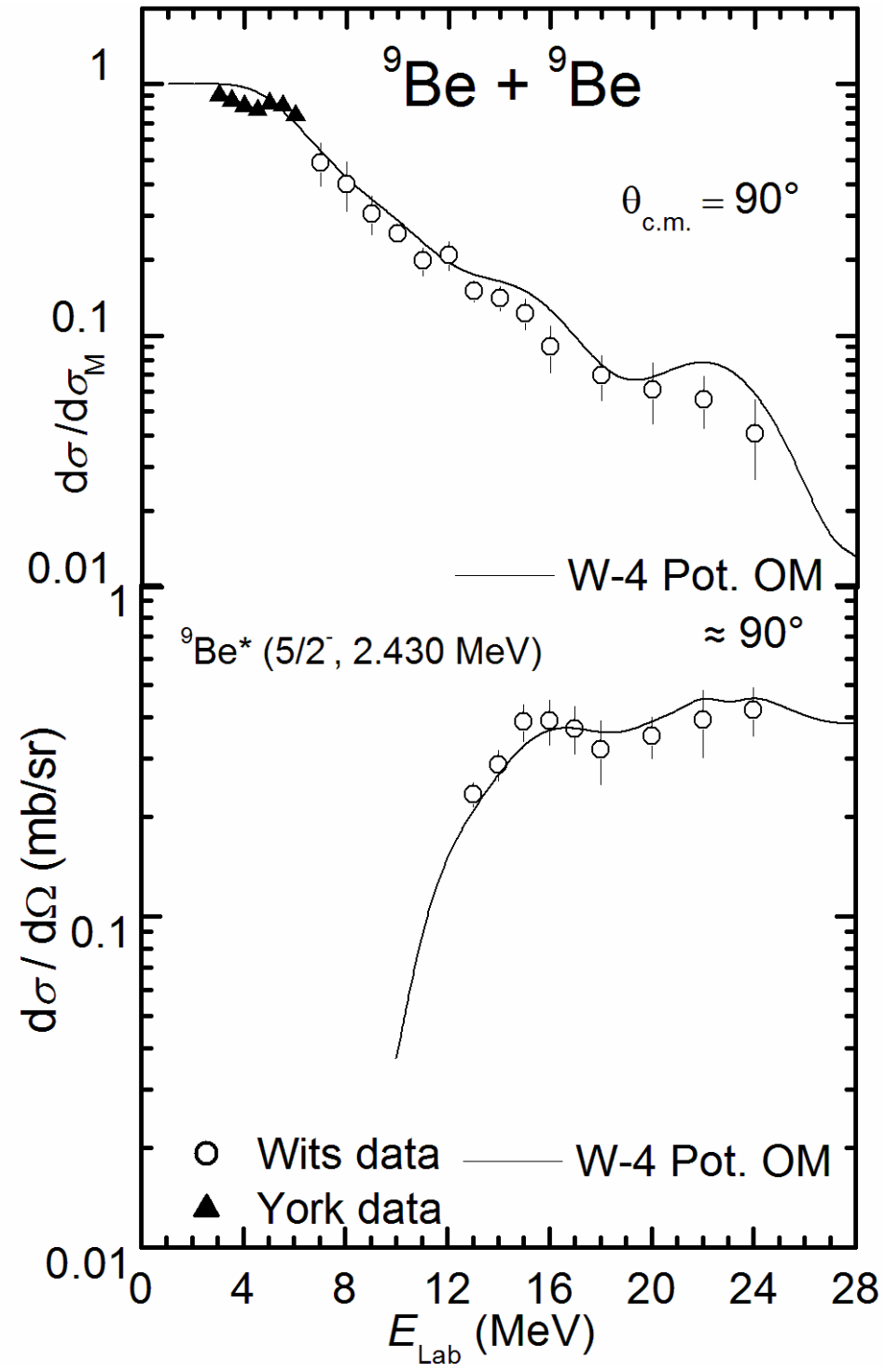


Figure 4.8: Upper part: Excitation functions for the elastic scattering of ^{9}Be + ^{9}Be at $\theta_{c.m.}$ = 90° for E_{Lab} = 7 to 24 MeV. Lower part: Inelastic excitation functions of ^{9}Be + ^{9}Be at $\theta_{c.m.}$ ≈ 90°. The data are fitted with the DWBA. Note that kinematically measurements can be made at an angle $\theta_{Lab.}$ = 45° only down to E_{Lab} = 9.5 MeV.

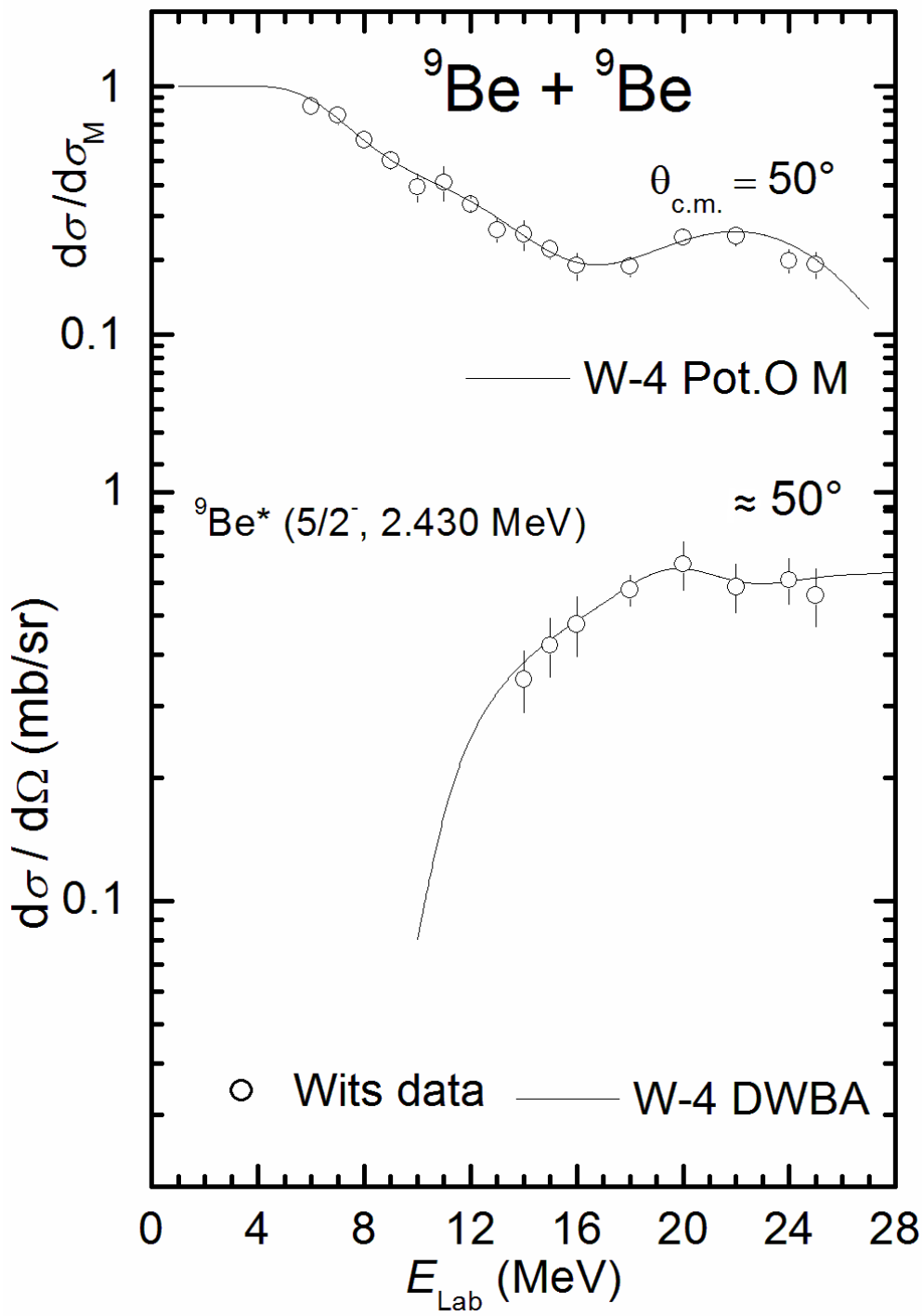


Figure 4.9: Upper part: Excitation functions for the elastic scattering of ^{9}Be + ^{9}Be at $\theta_{c.m.}$ = 50° for E_{Lab} = 7 to 24 MeV. Lower part: Inelastic excitation functions of ^{9}Be + ^{9}Be at $\theta_{c.m.}$ ≈ 50°. The data are fitted with the DWBA. Note that kinematically measurements can be made at an angle $\theta_{Lab.}$ = 25° only down to E_{Lab} below 6 MeV.

4.5 Discussion

The energy-dependent optical model potential found by York *et al*. [YO77] labelled C-1 to reproduces the gross features of the measured elastic scattering ^{9}Be + ^{9}Be for angular distributions at E_{Lab} = 5, 9, 12 and 16 MeV as seen in Fig. 4.2. The oscillating structure becomes more pronounced as the incident energy increases above the Coulomb barrier. A slightly better fit of the data at E_{Lab} = 16 MeV can be achieved by allowing V_0 and W_1 to vary (set W-1 of Table 4.1) as a consequence of an improved angular distribution measurement in comparison to that of York *et al*. [YO77].

Improved fits to the angular distribution data could be obtained by firstly allowing V_0 and W_1 to vary for each angular distribution (see Fig.4.3) and secondly by allowing the absolute normalisation of the data to vary (see Fig. 4.4). This resulted in a relatively small adjustment to the normalisation of the data by between 3% and 12% (set W-3 of Table 4.1). An energy-independent optical potential could then be found by averaging the values for V_0 and W_1 of set W-3 and allowing a simultaneous fit to be made for the all four angular distributions. The energy-independent optical potential is given by the set W-4 of Table 4.1 and the results of which are shown in Fig. 4.5 where it can be seen that good fits to the data are obtained.

Using the energy-independent optical potential set W-4, fits to the excitation function data at $\theta_{\mathrm{c.m.}}$ = 90° and 50° are shown in Fig. 4.6. Over the entire energy range measured from below to well above the Coulomb barrier at E_{Lab} = 6 to 25 MeV, respectively, the data are fitted very well together with oscillations in the data at the higher energy end.

The analysis is then extended to include a DWBA calculation for inelastic excitation to the second, unbound, state ^{9}Be*(5/2^{-}, 2.430 MeV). The results are

shown in Fig. 4.7 where it can be seen that the structure in the inelastic scattering data is reproduced very well. However, due to the limitations in the experimental measuring equipment, data above $\theta_{c.m.}$ = 102° could not be measured. Further measurements are necessary to ascertain if the cross-section would start to rise again at the more backwards scattering angles. The value of the deformation length extracted, δ_2 = 0.60 fm, is somewhat lower than that from in previous experiments e.g. proton inelastic scattering where δ_2 = 1.1 fm [VO73]. In addition, these values are lower than what would be expected when calculated from the B($E2\uparrow$) values where δ_2 = 2.0 fm. However, this is probably due to the limitation of the present DWBA analysis and coupled channels calculations [CO85] have produced δ_2 values close to that obtained B($E2\uparrow$) values.

Inelastic scattering data are also reproduced well by the excitation functions as seen in Fig. 4.8 and 4.9. Here, the measured cross-section rises steeply at the Coulomb barrier and flattens out as the incident energy increases.

Chapter 5

Summary and Conclusions

Measurements have been made of elastic scattering for the fermionic ^{9}Be + ^{9}Be system close to and above Coulomb barrier ($E_{\mathrm{Lab}}^{\mathrm{CB}}(^{9}\mathrm{Be}+{}^{9}\mathrm{Be}) = 8.0$ MeV). Cross sections have also been measured for inelastic scattering to the second unbound, state ^{9}Be*(5/2^{-}, 2.430 MeV). The angular distributions taken at E_{Lab} = 9, 12 and 16 MeV have been extended and superceded the very limited existing data at these incident energies for elastic scattering of ^{9}Be + ^{9}Be [YO77]. In addition, excitation functions for elastic scattering measured at $\theta_{\mathrm{c.m.}}$ = 50° and 90° from $6 \leq E_{\mathrm{Lab}} \leq 25$ MeV have again extended the very limited data from York *et al*. [YO77] taken at $\theta_{\mathrm{c.m.}}$ = 90°.

In the case of inelastic scattering, excitation of the second, unbound, state in ^{9}Be proceeds via a ΔL = 2 $\hbar$ transition from the ^{9}Be (3/2^{-}, g.s.) to ^{9}Be*(5/2^{-}, 2.430 MeV) in a two body reaction. After the interaction the excited ^{9}Be* breaks up ($^{9}\mathrm{Be}^{*} \rightarrow 2\alpha + n$) leaving the ground state ^{9}Be reaction partner to be detected. An angular distribution was measured for inelastic scattering at E_{Lab} = 16 MeV and two excitation functions at $\theta_{\mathrm{c.m.}} \approx 90°$ and 50° in the energy range $6 \leq E_{\mathrm{Lab}} \leq 25$ MeV. Such a complete set of inelastic scattering data at and just above the Coulomb barrier is not available in the literature.

Measurements were taken using a high-resolution gas-ionisation detector. The entrance window of 1 μm thick mylar into the isobutene gas of the gas-ionisation ΔE section limited the measurements to E_{Lab} (^{9}Be) ≥ 6 MeV. The maximum beam energy available at the time from the EN tandem Van de Graaff accelerator of iThemba LABS (Gauteng) of E_{Lab} (^{9}Be) = 25 MeV provided the upper limit.

Elastic scattering in the symmetric ^{9}Be + ^{9}Be fermionic system is sensitive to the ^{9}Be ground state spin of J^{π} = 3/2^{-} ħ, which is explicitly included in the Coulomb scattering formula (Mott scattering). In addition, anti-symetrization is required to

be included in the optical model of elastic scattering. In both cases, this leads to elastic scattering cross-sections that are symmetric around $\theta_{c.m.} = 90°$.

Starting from the energy-dependent optical potential of York *et al*. [YO77], an energy-independent optical potential was obtained by searching on the strength of the real and imaginary components V_0 and W_1, respectively. This was done by simultaneously fitting the angular distributions measured at E_{Lab} = 5, 9, 12 and 16 MeV. Indeed, over the limited incident energy range measured it is expected that an energy-independent optical potential is sufficient. Excellent fits were then obtained to excitation functions measured at $\theta_{c.m.} = 90°$ and 50° in the energy range $6 \leq E_{Lab} \leq 25$ MeV, using the energy-independent optical potential.

Turning to the inelastic scattering data, a good fit was achieved within the DWBA to the angular distribution measured at E_{Lab} = 16 MeV using the energy-independent optical potential. The extracted deformation parameter β_2 or deformation length (δ_2 = 0.6 fm) being consistent with the previous analyses [CO85], [OM84] and [VI93]. The inelastic-scattering excitation functions taken at $\theta_{c.m.} \approx 90°$ and 50° in the energy range $6 \leq E_{Lab} \leq 25$ MeV were also fitted well using the previously extracted deformation length.

Future work should include an angular distribution at the highest incident energy available (E_{Lab} (9Be) ≈ 29 MeV) for inelastic scattering to $^{9}Be^{*}(5/2^{-}$, 2.430 MeV) to access the more backward scattering angles $\theta_{c.m} \geq 102°$ not possible in the present measurement taken at E_{Lab} = 16 MeV due to scattered-particle energy limitations. As such, symmetry effects in the DWBA analysis can be investigated.

References

[AU78] E. H. Auerbach, A-Three: A general optical model code especially suited to heavy-ion calculations, Computer Physics Communications 15 (1978) 165-192.

[BE64] Sergio DeBenedetti, *Nuclear interactions* (John Wiley & Sons Inc. (1964) 74.

[CA78] J. M. Carter, *Inelastic scattering of heavy ions from light nuclei at energies near the coulomb barrier*, Doctor of Philosophy, University of the Witwatersrand, (1978).

[CO85] J. Cook and K. W Kemper, Phys. Rev. C31 (1985) 1745.

[FE91] H. Feshbach, *Theoretical Nuclear Physics* (John Wiley &Sons Inc. (1991) 8.

[FE92] R. W. Fearick, WIMPS 2 multi-parameter data acquisition system OS/2, Computer Programme (1992).

[FE54] H. Feshbach, C.E Porter and V F Wesskopf, Phys. Rev. (1954) 488

[JA70] D. F. Jackson, *Nuclear Reactions* (Methuen, London, 1970).

[JA85] L. Jarczyk, B. Kamys, A Magiera A Stralkowski, A Szczurek, K Bodek, M Hugi, J. Lang, R. Muller and E Ungright, Nucl. Physics. 11 (1985) 843-206.

[JE90] N. A. Jelley, *Fundamentals of Nuclear Physics*. Cambridge university Press 1990.

[JI10] M. Jingo, *Characteristics and use of a high resolution ΔE-E gas-ionisation detector for nuclear particle identification*, MSc Research Report, University of the Witwatersrand, (2010).

[HA89] E. Sideras-Haddad, *Elastic transfer process in the $^{12}C + ^{9}Be$ System.* MSc Dissertation, University of Witwatersrand, (1989).

[HO78] P. E. Hodgson, Nuclear heavy-ion reactions, (Oxford University Press, 1978).

[KR88] Kenneth S. Krane, *Introductory Nuclear Physics*, (John Wiley & sons, New York, 1988) 370-440.

[LE92] W. R. Leo, *Techniques for Nuclear and Particle Physics Experiments* (Springer-Verlag Berlin Heidelberg, 1992) 24-117.

[MA68] J. B. Marion and F. C. Young, *Nuclear Reactions Analysis* (North-Holland-Amsterdam, 1968) 39-41, 140-142.

[MO30] N. F. Mott, Proc. R. Soc. 126 (1930) 259.

[MU94] E. Muskat, PhD Thesis, *Inelastic scattering to unbound excited states in ^{6}Li and ^{9}Be*, University of Witwatersrand, 1994.

MU95] E. Muskat, J. Carter, R. W. Fearick and V. Hnizdo, Nucl. Phys. A581 (1995) 42-60.

[OM84] A. R. Omar, J. R. leigh, and T. R. Ophel, Phys.Rev.C30, (1984) 898.

[PO76] J.E. Poling, E. Norbeck and R. R. Carlson, Phys. Rev. C13 648.

[SA80] G. R. Satchler, *Introduction to Nuclear reactions*, Macmillan press Ltd 1980.

[UN79] E. Unright, D. Balzer, M. Hugi, J. Lang and R. Muller, Nucl. Phys A313 (1979) 376 – 384.

[VI74] F. Videbaek NBI, *Modified DWUCK for inelastic scattering*, 1974.

[VI85] M.F. Vineyard, J. Cook and K. W. Kemper, Phys. Rev. C31 (1985) 879.

[VI93] Z. Z. Vilakazi, *Cluster transfers between ^{9}Be and ^{12}C leading to bound and unbound states in the same system*, Msc Dissertation, University of the Witwatersrand, (1993).

[VO73] H. J. Votava, T. B. Clegge, E. J. Ludroig, and W. J. Thompson, Nucl. Phys. A204 (1973) 529.

[WI50] D. H. Wilkinson, *Ionisation Chambers and counter* (Cambridge Univ. Press. 1950) p 74-77.

[YO77] Richard C. York and R. T. Carpenter, Nucl. Physc. A282 (1977) 351.

Appendix-A

Tabulated values of the measured Quantities

Table A1: Elastic scattering of ^{9}Be + ^{9}Be at E_{Lab} = 16 MeV

$\theta_{\mathrm{c.m.}}$ (deg.)	$d\sigma / d\sigma_M$	**Error**
25.00	0.508	0.038
30.00	0.389	0.043
35.00	0.432	0.035
40.00	0.400	0.040
45.00	0.282	0.032
50.00	0.221	0.029
55.00	0.251	0.017
60.00	0.283	0.14
65.00	0.231	0.015
70.00	0.181	0.013
75.00	0.190	0.011
80.00	0.188	0.008
85.00	0.174	0.007
90.00	0.144	0.007
95.00	0.174	0.007
100.00	0.188	0.008
105.00	0.190	0.011
110.00	0.181	0.013
115.00	0.231	0.015
120.00	0.283	0.014
125.00	0.251	0.017
130.00	0.221	0.029
135.00	0.282	0.032
140.00	0.400	0.040
145.00	0.432	0.035
150.00	0.389	0.043
155.00	0.508	0.038

Table A2: Elastic scattering of ^{9}Be + ^{9}Be at E_{Lab} = 16 MeV (scaled data points)

$\theta_{\mathrm{c.m.}}$ (deg.)	$d\sigma / d\sigma_{M}$	**Error**
25.00	0.462	0.033
30.00	0.399	0.037
35.00	0.428	0.032
40.00	0.332	0.035
45.00	0.234	0.027
50.00	0.184	0.025
55.00	0.209	0.015
60.00	0.235	0.012
65.00	0.192	0.013
70.00	0.150	0.011
75.00	0.158	0.009
80.00	0.156	0.006
85.00	0.145	0.006
90.00	0.129	0.006
95.00	0.145	0.006
100.00	0.156	0.006
105.00	0.158	0.009
110.00	0.150	0.011
115.00	0.192	0.013
120.00	0.235	0.012
125.00	0.209	0.015
130.00	0.184	0.025
135.00	0.234	0.027
140.00	0.332	0.325
145.00	0.428	0.032
150.00	0.399	0.037
155.00	0.462	0.033

Table A3: Excitation functions of ^{9}Be + ^{9}Be at $\theta_{c.m.} = 50°$.

Energy (MeV)	$d\sigma / d\sigma_M$	**Error**
6.0	0.828	0.058
7.0	0.762	0.064
8.0	0.606	0.045
9.0	0.502	0.039
10.0	0.393	0.051
11.0	0.409	0.065
12.0	0.334	0.018
13.0	0.263	0.028
14.0	0.253	0.035
15.0	0.220	0.019
16.0	0.189	0.024
18.0	0.188	0.017
20.0	0.246	0.018
22.0	0.249	0.021
24.0	0.198	0.021
25.0	0.191	0.012

Table A4: Excitation functions of ^{9}Be + ^{9}Be at $\theta_{c.m.} = 90°$.

Energy (MeV)	$d\sigma / d\sigma_M$	**Error**
7.0	0.585	0.098
8.0	0.494	0.097
9.0	0.389	0.060
10.0	0.333	0.016
11.0	0.268	0.029
12.0	0.280	0.013
13.0	0.211	0.017
14.0	0.199	0.013
15.0	0.176	0.012
16.0	0.135	0.024
18.0	0.107	0.019
20.0	0.096	0.013
22.0	0.088	0.009
24.0	0.068	0.011

Table A5: Inelastic scattering of ^{9}Be + ^{9}Be at E_{Lab} = 16 MeV

Energy (MeV)	$d\sigma / d\Omega$ (mb/sr)	**Error** (mb/sr)
27.53	6.1	0.072
33.07	4.94	0.033
38.62	4.54	0.054
44.20	5.55	0.067
49.80	5.67	0.077
55.43	5.67	0.066
61.10	5.24	0.033
66.81	4.77	0.041
72.58	3.53	0.060
78.42	3.43	0.051
84.35	4.42	0.045
90.38	4.34	0.060
96.56	4.12	0.045
102.93	3.29	0.033

Table A6: Inelastic scattering of ^{9}Be + ^{9}Be at E_{Lab} = 16 MeV (scaled)

Energy (MeV)	$d\sigma / d\Omega$ (mb/sr)	**Error** (mb/sr)
27.53	5.3444	0.063
33.07	4.34	0.029
38.62	3.99	0.54
44.20	4.82	0.046
49.80	4.93	0.067
55.43	4.89	0.057
61.10	4.54	0.029
66.81	4.21	0.036
72.58	3.1	0.052
78.42	3.01	0.044
84.35	3.88	0.039
90.38	3.81	0.052
96.56	3.62	0.039
102.93	2.89	0.029

Table A7: Elastic scattering of ^{9}Be + ^{9}Be at E_{Lab} = 12 MeV

$\theta_{\mathrm{c.m.}}$ (deg.)	$d\sigma / d\sigma_{M}$	**Error**
30	0.671	0.059
35	0.532	0.067
40	0.479	0.072
45	0.421	0.071
50	0.388	0.076
55	0.301	0.077
60	0.228	0.066
70	0.300	0.075
80	0.293	0.068
90	0.199	0.044
100	0.293	0.068
110	0.300	0.075
120	0.228	0.066
125	0.301	0.077
130	0.388	0.076
135	0.421	0.071
140	0.479	0.072
145	0.532	0.067
150	0.671	0.059

Table A8: Elastic scattering of ^{9}Be + ^{9}Be at E_{Lab} = 12 MeV (scaled data)

$\theta_{\mathrm{c.m.}}$ (deg.)	$d\sigma / d\sigma_{M}$	**Error**
30	0.620	0.031
35	0.492	0.021
40	0.437	0.025
45	0.389	0.014
50	0.359	0.008
55	0.278	0.012
60	0.267	0.011
70	0.277	0.016
80	0.271	0.017
90	0.185	0.018
100	0.271	0.017
110	0.277	0.016
120	0.267	0.011
125	0.278	0.012
130	0.359	0.008
135	0.389	0.014
140	0.437	0.025
145	0.492	0.021
150	0.620	0.031

Table A9: Elastic scattering of ^{9}Be + ^{9}Be at E_{Lab} = 9 MeV

$\theta_{\mathrm{c.m.}}$ (deg.)	$d\sigma / d\sigma_{M}$	**Error**
30	0.929	0.033
35	0.833	0.066
40	0.789	0.061
45	0.600	0.055
50	0.521	0.077
55	0.399	0.080
60	0.466	0.041
70	0.390	0.066
80	0.379	0.056
90	0.310	0.042
100	0.379	0.056
110	0.390	0.066
120	0.466	0.041
125	0.399	0.080
130	0.521	0.077
135	0.600	0.055
140	0.789	0.061
145	0.833	0.066
150	0.929	0.033

Table A10: Elastic scattering of ^{9}Be + ^{9}Be at E_{Lab} = 9 MeV (scaled data)

$\theta_{\mathrm{c.m.}}$ (deg.)	$d\sigma / \mathrm{d}\sigma_M$	**Error**
30	0.888	0.033
35	0.796	0.066
40	0.688	0.061
45	0.523	0.055
50	0.498	0.077
55	0.381	0.08
60	0.378	0.041
70	0.335	0.066
80	0.355	0.056
90	0.296	0.042
100	0.355	0.056
110	0.335	0.066
120	0.378	0.041
125	0.381	0.08
130	0.498	0.077
135	0.523	0.055
140	0.688	0.061
145	0.796	0.066
150	0.888	0.033

Table A11: Inelastic scattering of ^{9}Be + ^{9}Be at E_{Lab} = 16 MeV and $\theta_{\mathrm{c.m.}} \approx 50°$

Energy (MeV)	$d\sigma / d\Omega$ (mb/sr)	**Error** (mb/sr)
12	0.321	0.051
13	0.330	0.061
14	0.349	0.052
15	0.423	0.041
16	0.476	0.036
18	0.577	0.027
20	0.667	0.036
21	0.587	0.025
22	0.611	0.038
24	0.559	0.040
25	0.559	0.043

Table A12: Inelastic scattering of ^{9}Be + ^{9}Be at E_{Lab} = 16 MeV and $\theta_{\mathrm{c.m.}} \approx 90$

Energy (MeV)	$d\sigma / d\Omega$ (mb/sr)	**Error** (mb/sr)
14	0.287	0.03
15	0.387	0.05
16	0.389	0.06
17	0.37	0.06
18	0.32	0.07
20	0.35	0.09
22	0.392	0.05
24	0.421	0.07

Table A13: Elastic scattering of ^{9}Be + ^{9}Be at E_{Lab} = 5 MeV [YO77]

$\theta_{c.m.}$ (deg.)	$d\sigma / d\sigma$	**Absolute Error** (mb/sr)
60	0.946	0.038
65	0.944	0.030
70	0.936	0.027
75	0.929	0.022
80	0.929	0.018
85	0.909	0.022
90	0.918	0.034
95	0.909	0.022
100	0.929	0.018
105	0.929	0.022
110	0.936	0.027
115	0.944	0.030
120	0.946	0.038

Appendix B

A copy of Nuclear Physics A282 York *et al*. [YO77]